August / août 2010 Volume/volume 104 Number/numéro 4 [743]

SUPPORT SCIENCE

Journal

The Journal of The Royal Astronomical Society of Canada

Le Journal de la Société royale d'astronomie du Canada

INSIDE THIS ISSUE

PROMOTING ASTRONOMY IN CANADA

August / août 2010

Journal

Vol. 104, No. 4 Whole Number 743

contents
table des matières

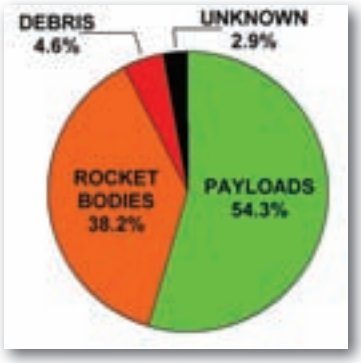

CASTOR Satellite Survey
p. 152

Astrocryptic Answers
p. 169

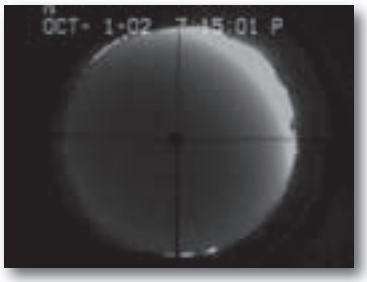

Atmospheric Height
by Twilight's Glow
p. 147

Pen & Pixel
p. 150

ROYAL ASTRONOMICAL SOCIETY OF CANADA

SOCIÉTÉ ROYALE D'ASTRONOMIE DU CANADA

DEPARTMENTS

The RASC at the Canada-Wide Science Fair
p. 170

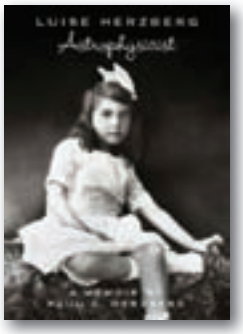

Book reviews
p. 171

Gizmos
p. 166

On the Front Cover:
Serge Théberge collected photons for a total of 13 hours to produce this spectacular image of IC 1871 in 2008 and 2009. Exposure was 13 x 15 minutes in H-alpha, 14 x 20 minutes in OIII emission, and 15 x 20 minutes in SII emission. Serge used a Takahashi FS-152 at f/8 and an SBIG ST-10XME camera from a site at Orangeville, Ontario. IC 1871 is a small 4-arcminute emission nebula in Cassiopeia and is associated with the much larger Heart and Soul Nebula.

COLUMNS

Executive Perspectives

by Mary Lou Whitehorne, President, RASC

The last time I sat down to write this column, the March 2010 National Council meeting had not yet been held. That meeting is now part of our history with the meeting minutes forming part of the official record of the life of the Society. That meeting will result in some fundamental and very positive changes for the RASC. Council voted in favour of hiring a paid, professional, Executive Director to attend to the many day-to-day management tasks that demand attention and action.

The ultimate goal we are striving for is a Society with renewed vision and strength, working together toward the common goals described in our Letters Patent:

(a) To stimulate interest and to promote and increase knowledge in astronomy and related sciences;
(b) To acquire and maintain equipment, libraries and other property necessary for the pursuit of its aims;
(c) To publish journals, books, and other material containing information on the progress of astronomy and the work of the Society;
(d) To receive and administer gifts, donations, and bequests from members of the Society and others;
(e) To make contributions and render assistance to individuals and institutions engaged in the study and advancement of astronomy.

The more immediate goal is release from the constant cycle of crisis management that arises from overburdened volunteers trying to run the Society's affairs on a part-time and as-available basis.

By the time you read this, this author will most likely be your President, and our new Executive Director will be installed and working hard at the National Office. Here I must beg everyone's indulgence in not looking for immediate and sweeping change to the Society. Change and improvement will come, but it will be incremental and slow. The first year or two will be primarily focused on establishing proper policy and procedure for the many activities that happen over the daily, weekly, monthly, and annual cycles of the RASC year. We will be establishing the foundation upon which more and greater things will be built by the RASC into our future.

ARE YOU MOVING? IS YOUR ADDRESS CORRECT?

If you are planning to move, or your address is incorrect on the label of your *Journal,* please contact the National Office immediately:

(416) 924-7973
www.rasc.ca/contact

By changing your address in advance, you will continue to receive all issues of *SkyNews* and the *Observer's Handbook.*

Journal

The *Journal* is a bi-monthly publication of The Royal Astronomical Society of Canada and is devoted to the advancement of astronomy and allied sciences. It contains articles on Canadian astronomers and current activities of the RASC and its Centres, research and review papers by professional and amateur astronomers, and articles of a historical, biographical, or educational nature of general interest to the astronomical community. All contributions are welcome, but the editors reserve the right to edit material prior to publication. Research papers are reviewed prior to publication, and professional astronomers with institutional affiliations are asked to pay publication charges of $100 per page. Such charges are waived for RASC members who do not have access to professional funds as well as for solicited articles. Manuscripts and other submitted material may be in English or French, and should be sent to the Editor-in-Chief.

Editor-in-Chief
Jay Anderson
203 – 4920 Dundas St W
Toronto ON M9A 1B7, Canada
Internet: editor@rasc.ca
Web site: www.rasc.ca
Telephone: (416) 924-7973
Fax: (416) 924-2911

Associate Editor, Research
Douglas Hube
Internet: dhube@phys.ualberta.ca

Associate Editor, General
Michael Attas
Internet: attasm@aecl.ca

Assistant Editors
Michael Allen
Martin Beech
Dave Chapman
Ralph Chou
Dave Garner
Patrick Kelly

Editorial Assistant
Suzanne E. Moreau
Internet: semore@sympatico.ca

Production Manager
James Edgar
Internet: jamesedgar@sasktel.net

Contributing Editors
Geoff Gaherty (Through My Eyepiece)
Dave Garner (On Another Wavelength)
Bruce McCurdy (Orbital Oddities)
Philip Mozel (A Moment With…)
Curt Nason (Astrocryptic)
Guy Nason (Carpe Umbram)
Andrew I. Oakes (News Notes)
Randall Rosenfeld (Art & Artifact)
Leslie Sage (Second Light)
Gerry Smerchanski (Gerry's Meanderings)
David Turner (Reviews)
Don van Akker (Gizmos)

Proofreaders
Ossama El Badawy
Margaret Brons
Angelika Hackett
Terry Leeder
Kim Leitch
Suzanne Moreau
Maureen Okun

Design/Production
Brian G. Segal, Redgull Incorporated

Advertising
James Edgar
Internet: jamesedgar@sasktel.net

Printing
Maritime Digital Colour

The *Journal of The Royal Astronomical Society of Canada* is published at an annual subscription rate of $94.50 (including tax) by The Royal Astronomical Society of Canada. Membership, which includes the publications (for personal use), is open to anyone interested in astronomy. Applications for subscriptions to the *Journal* or membership in the RASC, and information on how to acquire back issues of the *Journal* can be obtained from:

The Royal Astronomical Society of Canada
203 – 4920 Dundas St W
Toronto ON M9A 1B7, Canada
Internet: nationaloffice@rasc.ca
Web site: www.rasc.ca
Telephone: (416) 924-7973
Fax: (416) 924-2911

Canadian Publications Mail Registration No. 09818
Canada Post: Send address changes to 203 - 4920 Dundas St W, Toronto ON M9A 1B7

Canada Post Publication Agreement No. 40069313
We acknowledge the financial support of the Government of Canada through the Canada Periodical Fund (CPF) for our publishing activities.

Canada

The *Journal* is printed on recycled stock.

Incoming President Mary Lou Whitehorne poses with 100-mm eyepiece when visiting the DDO last fall. The eyepiece is on loan to the Toronto Centre from Orion Telescopes & Binoculars for their EPO programmes at the historic observatory. The photograph was taken by the R.A. Rosenfeld with a camera nearly as old as the DDO — at night without a flash!

This brings me to the bedrock upon which the Society foundations stand: our volunteers. Without you, our volunteers, there would be no RASC. We enjoy an unequalled international reputation for quality, authority, and integrity that has been built by RASC volunteers over our 142-year history. This is no small achievement!

Who are those volunteers? They are many, and I cannot name them all, but I do want to draw attention to some key volunteers without whom the Society would find itself in very difficult straits:

- The *Observer's Handbook* editor and 53 contributors, whose long hours of dedicated work bring us our chief source of charitable income every year, without fail. Much of our reputation rests on this annual publication.
- The *Journal* editor and production team of 30 volunteers, who also unfailingly produce six high-quality and interesting issues every year. It remains the only Canadian astronomical periodical of record. *JRASC* pages incorporate significant research works, including work on the history of Canadian astronomy. The *Journal* produces charitable income and contributes to our international standing as an astronomical organization of merit.
- The volunteer authors, editors, and contributors of our other publications (*Observer's Calendar, Beginning Observer's Guide,* and *Skyways*) also work long and tirelessly to produce these sources of charitable revenue for the Society, enabling us to fund and otherwise support public education programs across Canada.
- Members of National Council, committee chairs and members, Centre executive members, and every RASC member who contributes to Society meetings, activities, and events of all kinds across the country and beyond. You are the public face of the RASC, and you bring the Universe of astronomy to the people of Canada.

Every volunteer aspect of the RASC depends on all of the other volunteer contributions to make it all work. Members of the National Executive constantly watch the Society's vital signs and are keenly aware of, and deeply appreciate, the magnitude of the many contributions made by our key volunteers.

Over the years, we have been very successful in keeping our Society alive and thriving. The rapid pace of change in the RASC's working environment has brought us many challenges and many opportunities. As your President, I look forward to seeing the Society gain in strength, breadth, capacity, and reach as it moves into its new future.

The Royal Astronomical Society of Canada is dedicated to the advancement of astronomy and its related sciences; the *Journal* espouses the scientific method, and supports dissemination of information, discoveries, and theories based on that well-tested method.

Research papers
Articles de researche

Petrographic and Geochemical Analysis of the Shelburne Meteorite, an L5 Ordinary-Chondrite Fall

Katrina van Drongelen[1*], Kimberly Tait[2], George Clark[1], & Phil McCausland[3]

[1]Department of Geological Sciences, University of Manitoba, Winnipeg, Manitoba R3T 2N2 Canada
[2]Royal Ontario Museum, Department of Natural History, Toronto, Ontario M5S 2C6 Canada
[3]Department of Earth Sciences, University of Western Ontario, London, Ontario N6A 5B7 Canada
[*] current address: Department of Geology, University of Toronto, Toronto, Ontario M5S 3B1 Canada

Email Contact: k.vandrongelen@geology.utoronto.ca

Abstract: This study was undertaken to examine the Shelburne meteorite, which was observed to fall on 1904 August 13 near Shelburne, Ontario, with present-day techniques to expand the description of this Canadian meteorite and to reassess its L5 classification. Study of a 30-g sample provided by the Royal Ontario Museum included petrography, X-ray diffraction, and electron microbeam analysis to describe mineral occurrences, textures, and compositions. Several other Shelburne fragments have been investigated to determine bulk physical properties such as density, porosity, and magnetic susceptibility.

In Shelburne, the chondrules are moderately well delineated but not unaltered, suggesting a moderate degree of thermal metamorphism. Olivine shows irregular fractures, undulatory optical extinction, and planar fractures that suggest a moderate degree of shock metamorphism. Back-scattered electron (BSE) images and petrographic work reveal troilite and Ni-Fe metal phases to occur as independent subhedral grains, veins, and within chondrules. Powder X-ray diffraction (XRD) analysis of the bulk meteorite has identified the main mineral phases as Mg-rich olivine, low-Ca pyroxene, high-Ca pyroxene, plagioclase, troilite, and Ni-Fe metals. Electron Microprobe Analysis (EMPA) was used to examine the chemical variation in mineral species through the sample to determine the degree of equilibration. Olivine and pyroxene grains both show negligible variation in composition, indicating a high degree of equilibration in the Shelburne meteorite. The Shelburne meteorite is confirmed by this study to be an L5 chondrite with a moderate shock state of S3 and only minor weathering, W1. Shelburne has measured bulk properties that are similar to those expected for L chondrite falls.

1. Introduction

The Shelburne meteorite fell on 1904 August 13 in Ontario, Canada, and was named for the small town near which it fell (Borgström 1905). It was recovered shortly after the fall from two farms a few kilometres north of the town of Shelburne as two irregularly shaped pieces with masses of 12.6 kg and 5.6 kg (Borgström 1905; Farrington 1906). The meteorite is one of 58 meteorites to have been identified and officially recognized in Canada (MetSoc database 2010) as either a fall or find and is currently widely distributed in collections worldwide. A companion paper (McCausland & Plotkin 2009) reexamined the fall circumstances of the Shelburne meteorite and documented its subsequent distribution. As is the case for many Canadian meteorites, the century-old Shelburne meteorite lacks a modern comprehensive study (van Drongelen 2007); it is the aim of this paper to examine the Shelburne meteorite from a present-day perspective.

Chondritic meteorites are interpreted to have formed as an amalgamation of particles, many of which record different and diverse nebular histories (Brearly & Jones 1998). The study of chondrites is extremely important to understanding planetary-system formation and development because they offer insight into the earliest history of the solar nebula, hosting interstellar grains that survived processing in the solar-nebula environment. Typical chondrites are comprised of metallic phases, sulphides, silicate minerals, and sub-spherical chondrules (Table 1). By far the most common chondritic meteorite type to fall or be found is ordinary chondrite. Ordinary chondrites are classified as H-, L-, and LL-type based on "high," "low," and "very low" Fe-Ni metal content and more subtly on differences in the oxidation state of the iron (Figure 1; Rubin 1990).

Most chondrites have undergone secondary processing, such as heating and impact effects, to varying degrees in the nebula after the formation of their individual components or in their parent bodies after accretion (Hutchison 2004). Petrographic type, an integer from 1 to 6, is used to further delineate the different classes of chondrites, primarily on the basis of evidence for aqueous alteration and thermal metamorphism in the meteorite parent body (van Schmus & Wood 1967). Petrographic type 3 is taken to be the least altered; types 2 and 1 reflect aqueous alteration (observed in carbonaceous chondrites), whereas types 4 through 6 reflect increasing thermal metamorphism. The types are identified by textural features and mineral chemistry including a trend towards increased homogeneity (equilibration) of

Table 1 - Petrographic characteristics of chondrites (modified from Brearly and Jones 1998)

	Chondrule abundance[a] (vol%)	Matrix abundance (vol%)	Refractory inclusion abundance (vol%)	Metal abundance[b] (vol%)	Chondrule mean diameter (mm)
H	60-80	10-15	0.1-1?	10	0.3
L	60-80	10-15	0.1-1?	5	0.7
LL	60-80	10-15	0.1-1?	2	0.9
EH	60-80	<2-15	0.1-1?	8	0.2
EL	60-80	<2-15	0.1-1?	15	0.6
CI	<<1	>99	<<1	0	-
CM	20	70	5	0.1	0.3
CR	50-60	30-50	0.5	5-8	0.7
CO	48	34	13	1-5	0.15
CV	45	40	10	0-5	1
CK	15	75	4	<0.01	0.7
CH	~70	5	0.1	20	0.02
R	>40	36	0	0.1	0.4
K[c]	27	73	<0.1	0	0.6

[a] Chondrule abundance includes mineral fragments
[b] Metal abundance is for metal outside chondrules
[c] Matrix abundance includes metal

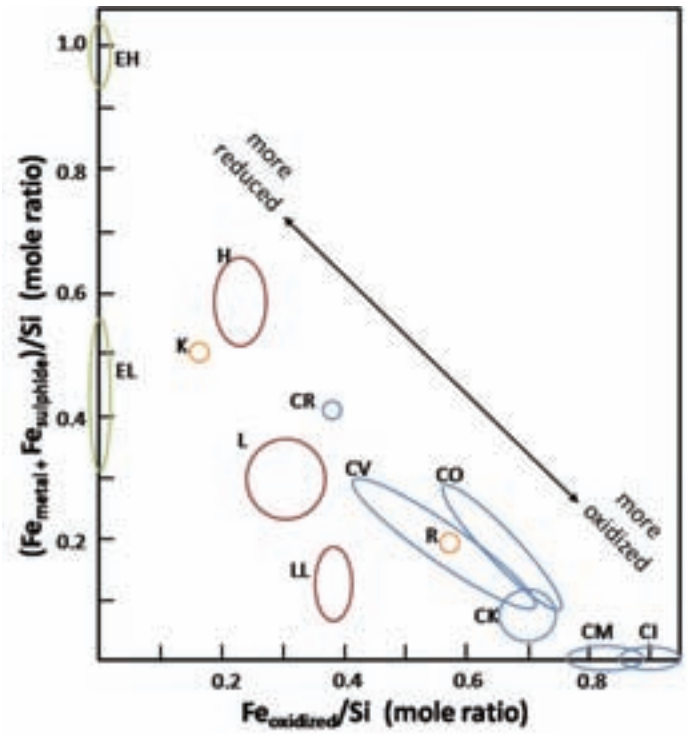

Figure 1 — Urey-Craig diagram showing relative Fe contents and oxidation states of the chondrite groups. Fe present in metal and sulphide phases plotted against Fe present in silicate and oxide phases for bulk chondrite compositions. The chondrite groups plot in discrete fields (modified from Brearley & Jones 1998).

olivine and pyroxene compositions with higher type number (Table 2). Fully equilibrated chondrites (type 6) have changed the most since their accretion into parent bodies, having experienced temperatures greater than 600 °C, just below the onset of partial melting (Brearly & Jones 1998).

2. Previous Work on Shelburne

Initial descriptions of the Shelburne meteorite appeared shortly after its fall, providing observations of the find circumstances for the two recovered fragments, descriptions of their physical appearance, petrographic descriptions, and bulk chemistry (Borgström 1905; Farrington 1906). Over the first half of the 20th century, pieces of both Shelburne fragments became widely distributed amongst museum, university, and private collections (McCausland & Plotkin 2009). Shelburne pieces thus became available for many synoptic studies of ordinary chondrite characteristics, despite the lack of a modern comprehensive study of the meteorite.

Mason (1963) used Shelburne in an X-ray diffraction study of the average fayalite content in olivine from approximately 800 chondrites to refine the classification scheme of Prior (King 1976). Shelburne was listed as having a mol percent fayalite (Fa) content of 24, fitting within the range of Fa_{22-31} of the olivine-hypersthene chondrites (Mason 1963).

Shelburne was one of eight L5 chondrites used in a study by Chou and Cohen (1973) on the gallium and germanium content of metal in L- and LL-chondrites. Chou and Cohen (1973) showed that there is a distinct separation of L- and LL-chondrites on a Ga vs. Ge plot and that the two elements are positively correlated in each chemical group.

Dodd and Jarosewich (1979) studied the incipient melting and

Table 2 - Summary of petrologic type criteria for chondrites (modified from Brearly & Jones 1998).

	Petrologic Type					
	1	**2**	**3**	**4**	**5**	**6**
Homogeneity of olivine and low-Ca pyroxene	-	>5% mean deviations		≤5%	homogeneous	
Structural state of low-Ca pyroxene	-	predominantly monoclinic		>20% monoclinic	<20% monoclinic	orthorhombic
Feldspar	-	minor primary grains only		secondary, <2 μm grains	secondary, 2-50 μm grains	secondary, >50 μm grains
Chondrule glass	-	altered, mostly absent	clear, isotropic, variable abund.		devitrified, absent	
Matrix	all fine-grained, opaque	mostly fine, opaque	clastic and minor opaque	transparent, recrystallized, coarsening from 4 to 6		
Chondrule-matrix integration	no chondrules	chondrules very sharply defined		chondrules well defined	chond. readily delineated	chondrules poorly defined

shock classification of L-group chondrites. Shelburne was classed as showing *d* facies shock metamorphism, using such criteria as fractured olivine with mosaic extinction and the deformation of plagioclase (Dodd & Jarosewich 1979). Shelburne did not have silicate melt veins, but melt pockets were observed in thin section. The ^{4}He and ^{40}Ar abundances measured for Shelburne as part of that study were 111 and 180 (x10^{-8} cm^{3} STP/g) respectively (Dodd & Jarosewich 1979). Localized melting can redistribute mobile elements, such as noble gases, in a chondrite. Those chondrites that have experienced significant shock, such as Shelburne, show depletion in ^{4}He and ^{40}Ar.

Jarosewich and Dodd (1985) included Shelburne in their study of the chemical variations among L-chondrites due to its unbrecciated nature and little evidence of shock melting. It was noted that Shelburne had low total-iron content, suggesting that it was an LL-chondrite, but its olivine iron content (Fa mol percent 22.7) confirmed that it was an L-chondrite (Jarosewich & Dodd 1985).

Shelburne has also been examined as a part of studies of meteorite gases (Schultz & Kruse 1989), to refine the classification of ordinary chondrites using kamacite and olivine (Rubin 1990); spectroscopic methods to determine asteroid mineralogy using meteorite compositional data (Berthoud *et al.* 2001); and in a comparison of the bulk chemistry of carbonaceous versus ordinary chondrites (Schoenbeck *et al.* 2006).

3. Shelburne Specimen Appearance

The main sample of the Shelburne meteorite for this study was provided by the Royal Ontario Museum (ROM) and in total weighed approximately 30 grams. This sample included a polished section, grains for destructive work (0.48 g), and two larger pieces (3.1 and 5.2 g; Figure 2). A thin section (30 microns thick) and a

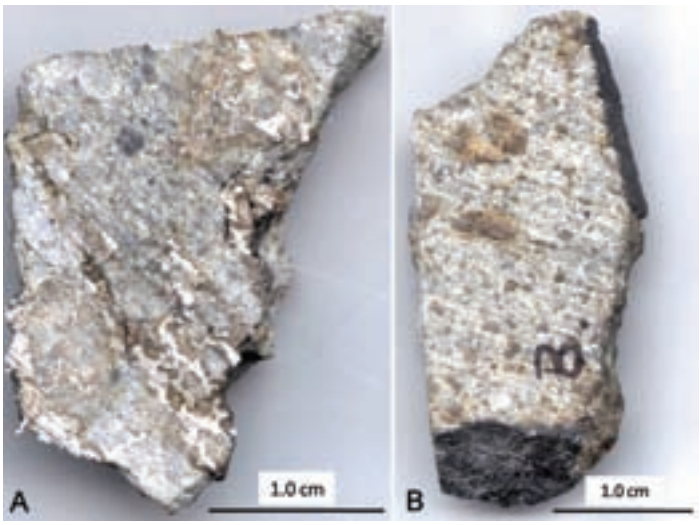

Figure 2 — Sample A has a mass of 5.2 g (3x2x0.3 cm) and sample B had a mass of 3.1 g (3x1.5x0.3 cm) prior to creation of thin sections. These are scanned images of the samples and were taken before thin sections were made of B. Sample A was used for SEM work. Sample A shows the distribution of chondrite material well; chondrules are visible on this scale, as are the metal and troilite. Sample B shows an older cut face, which is more oxidized. Also, note the black fusion crust visible on the top right and bottom (B).

Table 3 - Bulk physical properties for Shelburne meteorite fragments.

Fragment	Mass	Bulk Volume	Bulk Density	Grain Volume	Grain Density	Porosity	Magnetic Susceptibility	
	(g)	(cm^3)	(g/cm^3)	(cm^3)	(g/cm^3)	%	χ	log χ
UWO	80.22	23.73±1.68	3.38±0.24	22.65±0.12	3.54±0.02	4.55	95	4.98
Queen's	42.14	12.53±0.27	3.36±0.07	12.05±0.03	3.50±0.01	3.81	68.4	4.84
DG	30.32	9.03±0.32	3.36±0.12	8.69±0.13	3.49±0.01	3.75	131.8	5.12

Notes: Shelburne fragments are from the collections of the University of Western Ontario (UWO), Queen's University (Queen's), and David Gregory (DG); Bulk mass magnetic susceptibility χ is measured in SI units of 10^{-6} m^3/kg, and is reported here as the decimal logarithm of χ, taken as log 10^{-9} m^3/kg.

thick section (60 microns thick) were made from one of the larger pieces, whereas the other large piece was used for Scanning Electron Microscope (SEM) work and Back Scattered Electron (BSE) imaging. Three other pieces of Shelburne totalling 153 g, from the collections of University of Western Ontario (UWO), Queen's University (Queen's), and David Gregory (DG), underwent non-destructive analyses to determine Shelburne's bulk physical properties. Several larger pieces of Shelburne from the ROM collection were examined in hand sample.

The internal structure of the sample is heterogeneous with abundant dark chondrules comprising approximately 75 percent of the volume, as both broken and whole chondrules in varying states of definition. Sub-millimetre metallic grains are visible both surrounding and within the chondrules, and are oxidized on the outer surface of the sample due to prolonged exposure to air. Small metallic veins are visible macroscopically (fine <1-mm, and wider 1-3-mm veins).

The black fusion crust is visible in Figure 2B. In hand sample, the fusion crust is non-uniform, displaying irregular, rounded imprints with no distinct flow lines. Close to this fusion crust, troilite-filled hairline fractures were observed in Shelburne both in hand sample and thin section.

4. Shelburne bulk physical and mineralogical properties

Subsamples of Shelburne from the ROM with a total mass of 0.48 g were crushed to less than 1-mm grains for X-ray diffraction (XRD) analysis. A magnetic pick was used to separate the magnetic from the non-magnetic material. Data was collected on the two powder samples, one of primarily non-magnetic material and the other of primarily magnetic material, on a Phillips PW1710 powder diffractometer at the University of Manitoba. The magnetic component was analyzed on a quartz plate to decrease the background noise, whereas the non-magnetic component was analyzed on a regular glass slide. The two could not be completely isolated due to the intergrowth of the metallic and silicate phases as well as the malleability of the metallic phase, resulting in essentially identical X-ray diffraction patterns for the two sets of material. The bulk samples of the Shelburne meteorite are composed of kamacite, taenite, troilite, clinopyroxene, orthopyroxene, plagioclase feldspar, and forsterite.

Bulk physical properties for the Shelburne meteorite were measured for three fragments (Table 3): an 80-g fusion-encrusted slab (UWO collection), a 42-g triangular broken fragment with fusion crust and a ragged large-blade saw cut (Queen's collection), and an interior 30-g fragment with all irregular surfaces (DG collection). Images and other details on the history of these fragments can be found in McCausland and Plotkin (2009). Bulk density was measured using the Archimedean method employing a "liquid" of 40-μm glass beads (Consolmagno & Britt 1998; Consolmagno *et al.* 2008) in a repeatable fashion. A helium gas Quantachome Multipycnometer at UWO was used to determine the grain density of each of the fragments. Subtracting the grain volume from the bulk volume for each fragment allows its pore space to be calculated.

An average bulk density of 3.37 ± 0.01 g cm^{-3} is found for the three fragments. The grain density averages 3.51 ± 0.03 g cm^{-3} for the three fragments, in good agreement with the specific gravity of 3.499 g cm^{-3} determined by Borgström (1905) via the classic Archimedean water method on a 24-g fragment from the interior of the 12.6 kg stone. The porosity of Shelburne averages 4.0 percent, within the range of the 5.6 ± 4.7 percent porosity reported for other L chondrite falls (Consolmagno *et al.* 2008).

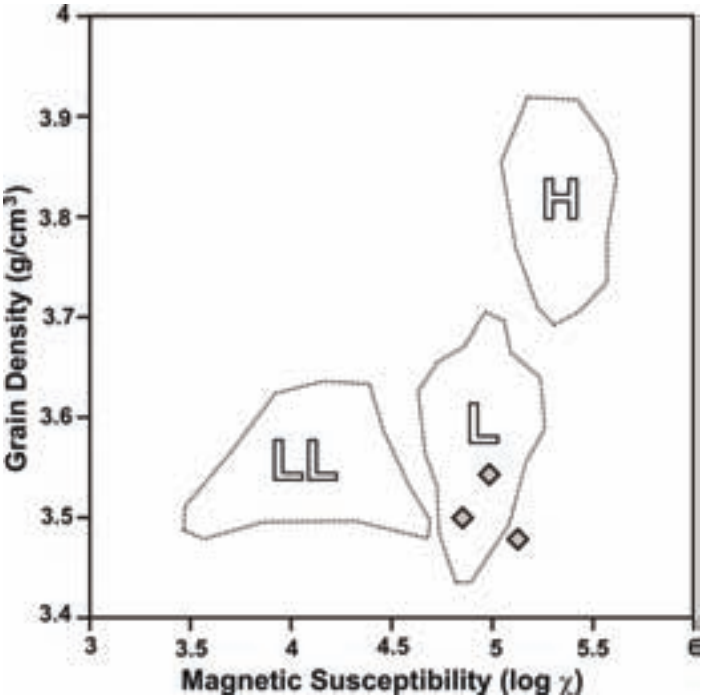

Figure 3— Grain density in g/cm^3 versus magnetic susceptibility in log χ for three Shelburne fragments (diamonds; Table 3), with reference to the distinct ranges of values for fragments from H, L, and LL meteorite falls (adapted from Consolmagno *et al.* 2006).

Magnetic susceptibility measurements were made using a Sapphire Instruments SI-2B susceptibility meter at UWO operating at 19,000 Hz and an applied field of 24 A/m (*e.g.* Rochette *et al.* 2003). Bulk mass magnetic susceptibility χ was recorded in SI units of 10^{-6} m^3kg^{-1} and checked against a standard composed of fine powder MnO_2. Following Rochette *et al.* (2003), we report the magnetic susceptibility χ, taken as log 10^{-9} m^3kg^{-1} for ease of comparison with other published data. The three Shelburne fragments differ slightly from one another, with the irregular fragment DG having the greatest susceptibility at log χ = 5.12, whereas the UWO and Queen's University fusion-encrusted cut-slab fragments have lower log χ values of 4.98 and 4.84, respectively. A comparison of the Shelburne fragment grain densities and magnetic susceptibilities with those published for ordinary chondrite falls (Consolmagno *et al.* 2006) confirms Shelburne to be an L chondrite (Figure 3).

5. Shelburne mineralogy and textures

The Shelburne meteorite is an ordinary chondrite containing abundant chondrules, visible metal, recrystallized glass, and a matrix composed of chondrule fragments, minor feldspar, and silicates. The components of Shelburne can be divided into three categories: 1) chondrules, 2) opaque phases, and 3) matrix. It is important to note that chondrites are heterogeneous in the distribution of their constituents and therefore the petrographic descriptions are approximations of the bulk meteorite and may vary between samples of Shelburne.

5.1 Chondrules

Petrographic work showed a variety of textural types of chondrules within the Shelburne sample, including granular, porphyritic, barred olivine, and radial chondrules (Hutchison 2004). The degree to which chondrules can be distinguished from the matrix material varies within the sample from moderate to poor due to some degree of thermal metamorphism in the Shelburne parent body. Many chondrules are broken, irregular in shape, or show cratered rims, reflecting differing nebular histories of the chondritic components prior to incorporation into their parent body. Overall, they constitute 75 vol percent of Shelburne (excluding chondrule fragments, which are considered part of the matrix material).

Granular chondrules are microcrystalline in nature, having an average crystal size of less than a few tenths of a millimetre (Figure 4A). They range in size from 0.5 to 1.3 mm in size, are sub-spherical in shape, and generally have irregular outlines. Granular chondrules in Shelburne feature numerous micro-craters, which occur only rarely in other chondrule types. This chondrule type constitutes 25 percent of the chondrules in Shelburne.

Porphyritic chondrules are the most abundant type in Shelburne and include olivine, pyroxene, and olivine-pyroxene porphyritic chondrules (Figure 4B). The division between the types is based on the ratio of olivine to pyroxene, being greater than 10 for porphyritic olivine, less than 0.1 for porphyritic pyroxene, and 0.1 to 10 for olivine-pyroxene chondrules (Hutchison 2004). The porphyritic olivine chondrules comprise 15 percent of the chondrules in Shelburne and range in size from 0.8 to 1.1 mm. They contain equaint and/or skeletal crystals of olivine that are anhedral to subhedral and 0.01 to 1.1 mm in size, in an aphanitic mesostasis. The porphyritic pyroxene chondrules make up 20 percent of the chondrules, are generally 1.0 mm in diameter, and consist primarily of anhedral to subhedral orthopyroxene crystals, 0.1 to 1.0 mm in diameter (± rare <0.1 mm olivine crystals). These chondrules generally have less mesostasis material than other porphyritic chondrule types. The porphyritic olivine-pyroxene chondrules constitute 20 percent of the chondrules and range in size from 0.4 to 1.3 mm in diameter. They contain orthopyroxene (equaint to elongate, 0.01 to 0.5 mm, and anhedral to subhedral), olivine (equaint or skeletal, 0.05 to 1.0 mm, and anhedral), ± clinopyroxene (0.05 to 0.1 mm and anhedral). Orthopyroxene is the most abundant phase in these chondrules and tends to be larger than and have overgrown the coexisting olivine and clinopyroxene.

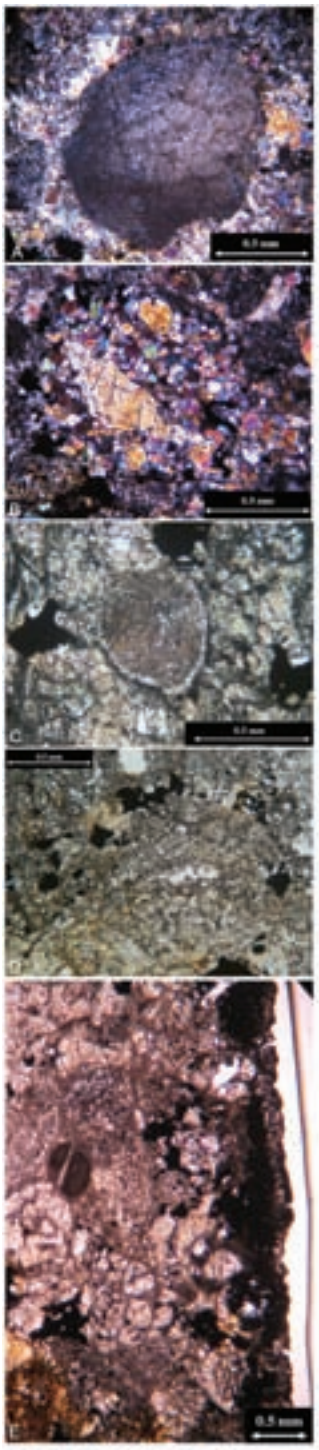

Barred olivine chondrules (Figure 4C) consist of parallel to sub-parallel plates of olivine, often surrounded by a continuous olivine shell. They range in size from 0.5 to 0.7 mm, are sub-spherical, and make up 10 percent of the Shelburne chondrules. The radial chondrules constitute 10 percent of the chondrules and range in size from 0.5 to 0.8 mm. They may have one or more nucleation sites near the chondrule rim and consist of thin orthopyroxene crystals in a sub-parallel, radiating pattern.

5.2 Opaque mineral phases

The opaque phases include troilite, kamacite, taenite, and

Figure 4 — (A) A moderately well-defined granular chondrule in cross-polarized light (XPL) displaying undulatory extinction and microcraters. (B) A porphyritic olivine-pyroxene chondrule in XPL featuring a large orthopyroxene crystal. (C) A rimmed barred-olivine chondrule in plain polarized light (PPL). (D) A PPL photo of metallic grains surrounding a chondrule. (E) A photomicrograph in PPL showing the heterogeneity of textures within the Shelburne sample, the varying types of chondrules present, the black fusion crust (along the right hand edge), the distribution of metallic and troilite grains, the varying degree of definition of the chondrules, and a fractured chondrule (likely due to shock).

iron-oxide and together constitute approximately 10 vol percent of Shelburne. Petrographic microscopy, SEM, and BSE imaging were used to examine the distribution of metals and sulphides within the Shelburne meteorite. Ni-Fe metal and troilite are present as grains surrounding chondrules and within select chondrules (Figures 3D & 5A-C). The troilite grains are generally smaller and are often located within Ni-Fe metal grains and veins; near the fusion crust, hairline fractures contain remobilized troilite.

Some grains appear to have been relatively unaltered subsequent to their incorporation into Shelburne as they contain no silicate inclusions, while others form around silicates and contain inclusions of them, suggesting remobilization and redistribution of some of the opaque phases in Shelburne.

There is also a minor degree of oxidation of the metal and sulphide material within the Shelburne meteorite. This is expressed as Fe-staining of surrounding silicate minerals (Figure 4E) and in the Ni-Fe grains as oxidation rims. Since Shelburne was recovered a short time after its fall and was not exposed to terrestrial weathering for long, the iron staining is relatively minor and is likely the result of post-fall humidity over the past century.

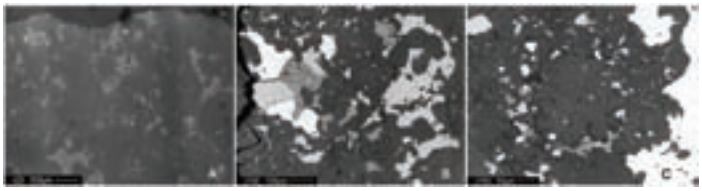

Figure 5 — (A) BSE image of Shelburne at low magnification showing brighter, disseminated metal and sulphide throughout the sample. (B) BSE image of Shelburne at a higher magnification. Three metallic phases can be identified (three levels of gray: white, light gray, and medium gray). In general, these are taenite, kamacite, and troilite respectively. (C) BSE image of the distribution of metallic and sulphide grains (kamacite/taenite and troilite) around a chondrule.

5.3 Shelburne matrix and textural relationships

The relative distribution of the different components of the Shelburne sample is quite varied. The diverse chondrule types are distributed randomly through the meteorite as can be seen in thin section (Figure 4E) and macroscopically in the larger pieces of the Shelburne meteorite (Figure 2). The degree to which the components are defined also varies through the sample (Figure 4E). Some of the chondrules, for example, are moderately well defined (Figure 4A), while others are broken or poorly defined (Figure 4D). This reflects different histories of the individual chondrules before accretion and alteration in the chondrite parent body.

Shelburne's matrix consists of fine olivine, pyroxene, plagioclase, troilite, taenite, and kamacite, all acting as a host to whole and broken chondrules and a few larger silicate grains, not unexpected for chondritic matrix (McSween 2000). The degree of thermal metamorphism (leading to chemical equilibration) can be estimated based on petrographic textures. The glass throughout the sample is devitrified and it has crystallized to form feldspar. The observed coarsening of matrix and resultant obscuring of chondrule outlines is characteristic of a high degree of thermal metamorphism (van Schmus & Wood 1967; McSween 2000).

Fractures through chondrules are visible in Shelburne and are indicative of shock metamorphism (Figure 4E). Shelburne also contains thin silicate melt veins, indicative of a moderate degree of shock (Stöffler *et al.* 1991). The olivine in Shelburne exhibit irregular fractures, undulatory extinction, and fine planar fractures, which together denote a shock classification of S3 (Table 4).

6. Mineral chemistry by EMPA Analyses

A Cameca SX-100 was used for Electron Microprobe Analysis (EMPA) to examine the chemistry, degree of equilibration, and the relative distribution of Fe, Ni, S, and Mg between the silicate and opaque phases in the Shelburne meteorite. The 60-micron-thick

Table 4 - Shock classification for ordinary chondrites (modified from Stöffler et al. 1991).

Shock Stage	**Effects of equilibration peak shock pressure** *Olivine*	*Plagioclase*	**Local Effects**	**Shock Pressure (GPa)**
S1 Unshocked	Sharp optical extinction, irregular fractures		none	<4-5
S2 Very weakly shocked	Undulatory extinction, irregular fractures		none	5-10
S3 Weakly shocked	Planar fractures, undulatory extinction, irregular fractures	Undulatory extinction	Opaque shock veins, minor melt pockets, may be interconnected	10-15
S4 Moderately shocked	Mosaicism (weak), planar fractures	Undulatory extinction, partially isotropic, planar deformation features	Melt pockets, interconnected melt veins, opaque shock veins	25-30
S5 Strongly shocked	Mosaicism (strong), planar fractures + planar deformation features	Maskelynite	Pervasive melt pockets, veins, and dikes; opaque shock veins	45-60
S6 Very strongly shocked	Restricted to local regions in or near melt zones		Pervasive melt pockets, veins, and dikes; opaque shock veins	75-90
	Solid state recrystallization, ringwoodite, melting	Shock melted (normal glass)		
Shock melted	Whole rock melting (impact melt rocks and melt breccias)			

section used for this analysis was carbon coated and taped to the stage with a magnetism-reducing tape. A total of 14 minerals were analyzed, each with 3 data points, including 7 pyroxenes, 4 olivines, 1 feldspar, 1 chromite, and 1 phosphate mineral (van Drongelen 2007).

Olivine and pyroxene individual-grain compositions from the Shelburne meteorite, obtained through EMPA analyses as part of this study, fall within expected values for an L-type ordinary chondrite of Fa = 22-26 and Fs = 19-22 (Figures 6, 7, and 8; Brearly & Jones 1998). Note that the olivines plot in a tight cluster (Fa = 23.77 ± 0.19), which is indicative of an advanced degree of chemical equilibration. The pyroxenes plot in two fairly distinct groups, also suggesting a moderate to advanced degree of equilibration (Brearly & Jones 1998). There is a group of Ca-rich pyroxene (Wo_{34-47}), a group of Ca-poor pyroxene (Wo_{0-3}), and a minor amount of intermediate pyroxenes (Wo_{5-20}). The presence of augite indicates that Shelburne has not experienced metamorphism as high as petrologic type 6, while the low-Ca pyroxene compositions (Fs = 20.26 ± 0.04) indicate a moderate to high degree of equilibration (Brearly & Jones 1998).

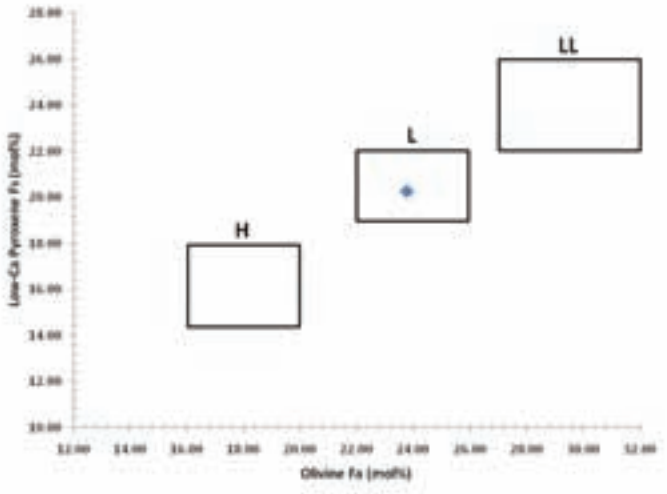

Figure 6 — The average low-Ca pyroxene and olivine of Shelburne plot within the expected values for type L ordinary chondrites (Brearly & Jones 1998).

A set of qualitative X-ray maps were created for an area of the Shelburne meteorite that featured a representative distribution of silicate and Ni-Fe metal and sulphide phases (Figure 9). The relative distributions of Mg, Ni, S, and Fe were mapped, showing fairly uniform compositions within single grains (*i.e.* a lack of zoning or chemical alteration of parts of grains), consistent with chemical equilibration having taken place.

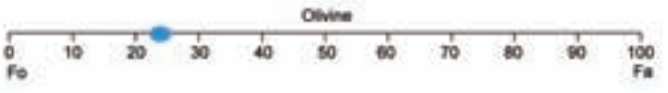

Figure 7 — Olivine compositions of Shelburne (mol percent). Chondrule olivine data from Shelburne plot in a tight grouping, a well-equilibrated distribution (Fa = 23.77 ± 0.19).

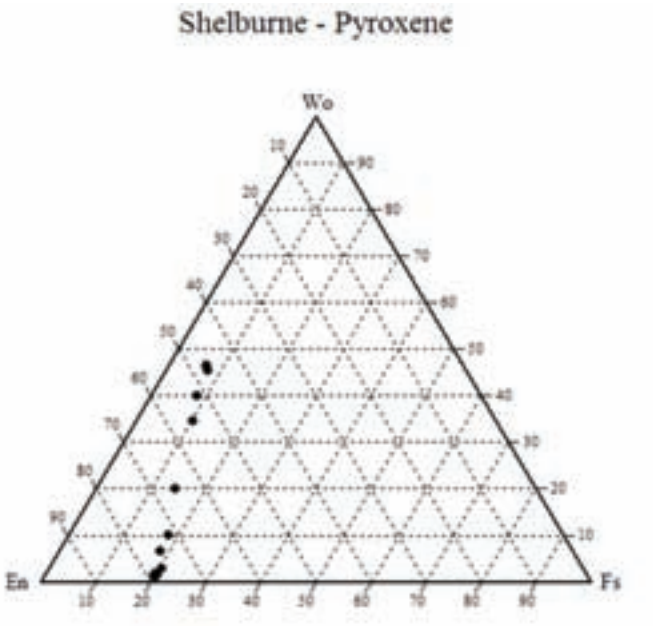

Figure 8 — Plot of seven pyroxenes of chondrules in Shelburne (mol percent). There are two distinct groupings of pyroxenes in this data set, Ca-rich (Wo=38.79 ± 10.26) and Ca-poor (Fs= 20.26 ± 0.04). Intermediate compositions (Wo_{5-20}) are pigeonite, which are often present in minor amounts in equilibrated ordinary chondrites (Brearly & Jones 1998).

It can be readily observed that the distribution of Mg is restricted to the silicate part of the sample and is present in variable amounts (olivine and pyroxene). The Ni map defines the Ni-Fe metal phase of the sample, as Fe is present in all of the metal, sulphide, and silicate phases. The small grain with an elevated Ni content (upper-left part of the image) is likely taenite ($Fe_{<0.8}Ni_{>0.2}$), rather than kamacite ($Fe_{>0.9}Ni_{<0.1}$). Kamacite has a lower Ni content relative to taenite and appears blue on the Ni X-ray map. The sulphur map shows the distribution of the troilite (FeS) in the sample. This corresponds with the Fe distribution of moderate abundance. It is important to note that the troilite appears to contain significant inclusions of silicates while the Ni-Fe alloys contain very few inclusions, suggesting that the troilite may have been more mobile relative to Ni-Fe metal.

7. Discussion and Conclusions

Shelburne consists of moderately well-defined chondrules, opaque phases, and matrix material. The degree to which chondrules can be distinguished from matrix material, composed of poorly defined broken chondrule fragments and recrystallized glass, is a reflection of the degree of thermal alteration while part of the L-chondrite parent body. Petrographic work showed a variety of textural types of chondrules within Shelburne, including porphyritic, barred-olivine, radial-pyroxene, and granular chondrules.

In the literature, granular chondrules have also been termed microcrystalline and microporphyritic. Relative to their porphyritic counterparts, the granular chondrules form due to a greater abundance of nucleation sites, rather than differing cooling rates (Hewins 1983). Through experiments outlined in Hewins' (1983) work, the olivine microporphyry was simulated in two ways: 1)

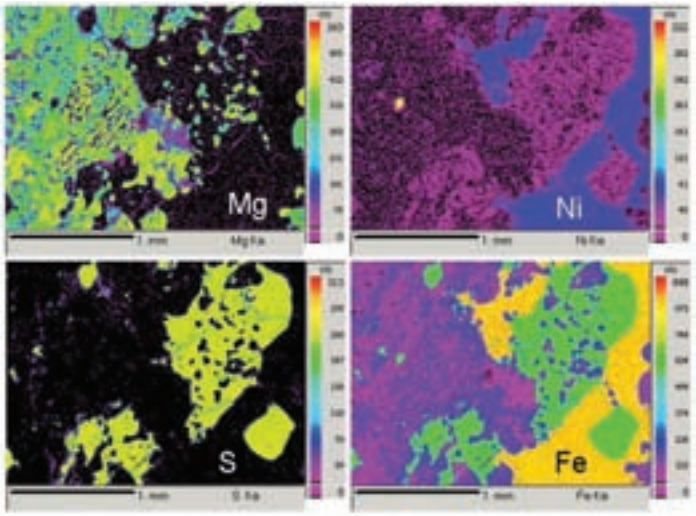

Figure 9 — EMPA X-ray maps of Shelburne showing the relative distribution of Mg, Ni, S, and Fe. See text for discussion.

cooled from above the liquidus at low rates and 2) cooled from just below the liquidus at moderately high rates. Alternatively, they may have formed by crystallization from incompletely melted pre-existing mineral clusters, with these relict minerals acting as nucleation sites (Nagahara 1983).

Porphyritic chondrules tend to be rich in siderophile elements relative to non-porphyritic chondrules (Grossman & Wasson 1983). These chondrules are thought to have formed through a process of remelting and recrystallization, evidence of which has been noted by relict crystals within porphyritic crystals (Nagahara 1983). Barred olivine chondrules tend to be depleted in metal (Grossman & Wasson 1983). These are also thought to have formed from a remelting process and recrystallization before aggregation into a parent body (Nagahara 1983). Barred olivine chondrules are typically less common than porphyritic chondrules in ordinary chondrites (Wasson, 1985).

Interstitial material (mesostasis), usually glass, commonly devitrifies due to thermal metamorphism, as in the case of the Shelburne chondrules. The small crater-like indentations observed in several chondrule types, and especially in granular chondrules, form either by low-velocity collisions between chondrules prior to accumulation in the chondrite parent body or by post-solidification loss of metal or sulphide droplets from the surface (Wasson 1985).

Fractures through chondrules are visible in Shelburne and are indicative of shock metamorphism. The mineral and chondrule fractures likely resulted from shock within the parent body and the shock when Shelburne was ejected from its parent body. There is significant recrystallization along these fractures, suggesting a relatively deep location of the sample within the parent body that was impacted at a relatively early time while the parent body was still undergoing thermal metamorphism. The olivine in Shelburne displays irregular fractures, undulatory extinction, and fine planar fractures. These observations, along with the presence of melt-veins, indicate that Shelburne is shock stage S3 (Table 4).

The opaque phases include troilite, kamacite, taenite, and Fe-oxide, which were observed by reflective microscopy and BSE imaging as grains within and surrounding chondrules, as well as hairline fractures near the fusion crust. Shelburne exhibits a mild degree of weathering from post-fall humidity since it fell over a century ago. Minor oxide rims surround metal and troilite in the sample, characteristic of weathering stage W1 (Table 5; Wlotzka, 1993).

Fe-Ni metal and troilite veins of greater than 1-mm thickness are visible in the slice examined by SEM (Figure 2). These veins do not occur in the piece from which the polished thin section was made, and are observed to occur only occasionally in other fragments of Shelburne (McCausland & Plotkin 2009). In the initial physical description of a complete 12.6-kg individual Shelburne meteorite, Borgström (1905) noted the presence of mm-sized metal-troilite veins which passed entirely through the meteorite. Texturally, the vein examined in this study appears to invade and envelop silicate grains implying that it is a "late" feature, consistent with remobilization of the metal and sulphides in the meteorite parent body during shock metamorphism (Stöffler *et al.* 1991).

Shelburne is comprised of forsterite, clinopyroxene, orthopyroxene, plagioclase, kamacite, taenite, and troilite, as observed by XRD and EMPA. The olivine in Shelburne exhibits a small variation in chemistry and the pyroxene plot in two fairly restricted areas, but include minor intermediate compositions (pigeonite and augite). The data obtained from this study are consistent with the classification of the Shelburne meteorite as an L5 ordinary chondrite.

The degree of thermal metamorphism of a meteorite is a function of depth. The internal temperature that a parent body may reach and maintain for a significant period of time at a given depth is dependent on the size of the body. With increasing degree of thermal metamorphism, a chondrite will experience devitrification of glass, recrystallization, and chemical equilibration. L5 chondrites are thought to represent relatively deeper portions of an L-chondrite parent body (Brearly & Jones 1998).

Several conclusions can be made regarding the classification of the Shelburne meteorite as a result of this study:

1. It is an L-type ordinary chondrite
2. It experienced a moderate-high degree of thermal metamorphism while part of its parent body and has equilibrated to petrographic type 5
3. It has undergone a low degree of shock, S3
4. It has experienced a minor amount of post-fall weathering, W1

Table 5 - Weathering scale (modified from Hutchison 2004).

Weathering Scale	
W0:	No visible oxidation
W1:	Minor oxide rims around metal and sulphide; minor oxide veins
W2:	~20-60 vol% metal affected by oxidation; veining with Fe oxides common
W3:	Heavy oxidation; 60-95% of metal and sulphide replaced
W4:	Complete (>95%) oxidation of metal and sulphide; silicates remain unaffected
W5:	Mafic silicates slightly altered, mainly along cracks; olivines tend to alter from within
W6:	Massive replacement of silicates by clay minerals and oxides

Glossary of Terms

Aphanitic: The term used to describe a grain size that is too fine to be distinguished by eye.
Barred Chondrule: Dendritic olivine of elongate, platy, subparallel crystals, separated by a glassy mesostasis, enclosed by a olivine rim from which olivine plates grew inwards (pyroxene may also exhibit this texture ± olivine) (Hutchison 2004).
Chondrule: Spherules, mm-sized, comprised primarily of silicates, and rarely metal and/or sulphide, which are believed to have been formed by the melting and re-solidification of material in microgravity environments in the early Solar System (Hutchison 2004).
Devitrification: The process of crystallization of a previously amorphous glass.
Granular Chondrule: Chondrule comprised of submicroscopic crystals of pyroxene (Hutchison 2004). For this study, crystal sizes of up to 400 µm were considered granular if grain size was uniform and no significant mesostasis was present.
Kamacite: One of two major Ni-Fe alloys in chondrites with composition $Ni_{<10\%}Fe_{>90\%}$
Liquidus: The maximum temperature at which crystals can coexist with liquid in equilibrium.
Magnetic susceptibility: The magnetic susceptibility of a meteorite is a measure of its magnetic response to an externally applied magnetic field; it is a function of magnetic mineralogy such as kamacite and magnetite in the meteorite (Rochette *et al.* 2003).
Maskelynite: Glassy phase with a composition similar to plagioclase formed by shock melting in a meteorite (Stöffler *et al.* 1991).
Mosaicism: Mechanical deformation of a crystal due to shock resulting in a mottled appearance at extinction under a polarizing microscope (Stöffler *et al.* 1991).
Olivine: A magnesium-iron silicate with the general formula $(Fe,Mg)_2SiO_4$ that varies in composition between magnesium (Forsterite: Fo) and iron (Fayalite: Fa) end-members.
Plagioclase: A feldspar mineral with compositional range $NaAlSi_3O_8$ to $CaAl_2Si_2O_8$.
Porphyritic Chondrule: Optically resolvable elongated to equaint crystals of pyroxene and/or olivine set in a fine-grained, cryptocrystalline, or glassy mesostasis in a parallel or radiating orientation (Hutchison 2004).
Pyroxene: Silicate mineral with the general formula $XY(Si,Al)_2O_6$ where X represents Fe^{2+}, Ca, Na, and Mg and Y represents Fe^{3+}, Al, and Cr. Pyroxenes are usually divided into orthopyroxenes, those that are in the orthorhombic crystal system, and clinopyroxenes, those that are in the monoclinic crystal system. Orthopyroxenes in general have low-Ca content relative to the clinopyroxenes. Wollastonite (Wo) is the Ca-rich end-member, Ferrosilite (Fs) the Fe-rich end-member, and Enstatite (En) is the Mg-rich end-member.
Radial Pyroxene Chondrule: Fibrous pyroxene crystals of low-Ca pyroxene that radiate from one or more points on or near the chondrule margin (Hutchison 2004).
Siderophile: The term used to describe an element with a strong affinity for iron.
Subhedral: The intermediate term describing how well crystal faces are developed between ***euhedral*** (well formed) and ***anhedral*** (poorly formed).
Taenite: One of two major Ni-Fe alloys in chondrites with composition $Ni_{>20\%}Fe_{<80\%}$
Troilite: The primary sulphide phase in meteorites consisting of FeS

8. Acknowledgements

The authors would like to thank Sergio Mejia, Panseok Yang, and Neil Ball (University of Manitoba) for their assistance in the instrumental analysis; Ian Nicklin (Royal Ontario Museum) for his assistance with the samples; Mark Badham (Queen's University) and David Gregory for kindly loaning Shelburne samples for bulk properties measurements; Currie Palmer (University of Western Ontario) for assistance with the magnetic susceptibility measurements; and Graham Wilson from Turnstone Geological Services for providing assistance with the literature search of the Shelburne meteorite. Additionally the authors would like to recognize the Fawcett & Gittins Graduate Explorers Fund and the University of Toronto for their financial support.

References

Berthoud, M.G., Bell III, J.F., and Clark, B.E. (2001). Testing spectral methods for asteroid surface compositional determination using spectroscopic and compositional data of ordinary chondrite meteorites. *32nd Annual Lunar and Planetary Science Conference,* March 12-16 Houston, Texas, abstract no. 2080

Borgström, L.H. (1905). The Shelburne meteorite. *JRASC,* 69-94.

Brearley, A.J. & Jones, R.H. (1998). Chondritic Meteorites. In J.J. Papike (Ed.), *Planetary Materials* (pp. 3-01 - 3-370). *Vol. 36. Reviews in Mineralogy.* Washington, D.C.: Mineralogical Society of America.

Chou, C.L. & Cohen, A.J. (1973). Gallium and germanium in the metal and silicates of L- and LL-chondrites. *Geochimica et Cosmochimica Acta, 37,* 315-327.

Consolmagno, G.J. & Britt, D.T. (1998). The density and porosity of meteorites from the Vatican collection, *Meteoritics & Planetary Science, 33,* 1231-1241.

Consolmagno, G.J., Macke, R.J., Rochette, P., Britt, D.T., & Gattacceca, J. (2006). Density, magnetic susceptibility, and the characterization of ordinary chondrite falls and showers, *Meteoritics & Planetary Science, 41,* 331-342.

Consolmagno, G.J., Britt, D.T. & Macke, R.J. (2008). The significance of meteorite density and porosity, *Chemie der Erde, 68,* 1-29.

Dodd, R.T. and Jarosewich, E. (1979). Incipient melting and shock classification of L-Group chondrites. *Earth and Planetary Science Letters, 44,* 335-340.

Farrington, O.C. (1906). The Shelburne and South Bend Meteorites, *Field Columbian Museum, Publ., 109,* 7-17.

Grossman, J.N. & Wasson, J.T. (1983). The compositions of chondrules in unequilibrated chondrites: An evaluation of models for the formation of chondrules and their precursor materials. In E.A. King (Ed.), *Chondrules and their origins* (pp. 88-121). Houston, Texas: Lunar and Planetary Institute.

Hewins, R.H. (1983). Dynamic crystallization experiments as constraints on chondrule genesis. In E.A. King (Ed.), *Chondrules and their origins* (pp. 122-133). Houston, Texas: Lunar and Planetary Institute.

Hutchison, R. (2004). *Meteorites: A Petrologic, Chemical, and Isotopic Synthesis.* Cambridge, UK: Cambridge University Press.

Jarosewich, E. & Dodd, R.T. (1985). Chemical variations among L-chondrites - IV. analysis, with petrographic notes, for 13

L-Group and 3 LL-Group chondrites. *Meteoritics, 20,* 23-36.

King, E.A. (1976). *Space geology: an introduction.* New York, USA: John Wiley & Sons.

Korochantseva, E.V., Trieloff, M., Lorenz, C.A., Buykin, A.I., Ivanova, M.A., Schwarz, W.H., Hopp, J., and Jessberger, E.K. (2007). L-chondrite asteroid breakup tied to Ordovician meteorite shower by multiple isochron 40Ar-39Ar dating. *Meteoritics and Planetary Science, 42,* 113-130.

Mason. B. (1963). Olivine composition in chondrites. *Geochimica et Cosmochimica Acta, 27,* 1011-1023.

McCausland, P.J.A. and Plotkin, H. (2009). *JRASC, 103*, 181-188.

McSween, Jr., H.Y. (2000). *Meteorites and their parent planets.* Cambridge, UK: Cambridge University Press.

MetSoc, 2010. The Meteoritical Bulletin Database: Shelburne. *The Meteoritical Society.* < http://tin.er.usgs.gov/meteor/metbull.php?code=23529>, [2010 April 2].

Nagahara, H. (1983). Chondrules formed through incomplete melting of the pre-existing mineral clusters and the origin of chondrules. In E.A. King (Ed.), *Chondrules and their origins* (pp. 211-222). Houston, Texas: Lunar and Planetary Institute.

Nesvorný, D., Vokrouhlický, D., Morbidelli, A., & Bottke, W.F. (2009). Asteroidal source of L chondrite meteorites. *Icarus, 200,* 698-701.

Rochette, P., Sagnotti, L., Bourrot-Denise, M., Consolmagno, G., Folco, L., Gattacceca, J., Osete, M.L. & Personen, L. (2003). Magnetic classification of stony meteorites: 1. Ordinary chondrites. *Meteoritics & Planetary Science, 38,* 251-268.

Rubin. A.E. (1990). Kamacite and olivine in ordinary chondrites: intergroup and intragroup relationships. *Geochimica et Cosmochimica Acta, 54,* 1217-1232.

Schoenbeck, T.W., Zipfel, J., and Palme, H. (2006). Bulk chemistry of carbonaceous and ordinary chondrites, a comparison. *37th Annual Lunar and Planetary Science Conference,* March 13-17, League City, Texas, abstract no. 1817

Schultz, L.L. & Kruse, H. (1989). Helium, neon, and argon in meteorites – a data compilation. *Meteoritics, 24,* 155-172.

Stöffler, D., Keil, K., & Scott, E.R.D. (1991). Shock metamorphism of ordinary chondrites. *Geochimica et Cosmochimica Acta, 55,* 3845-3867.

van Drongelen, K.D. (2007). Petrographic and geochemical analysis of the Shelburne meteorite, an L5 ordinary chondrite fall. Unpublished Manuscript, University of Manitoba.

van Schmus, W.R. & Wood, J.A., (1967). A chemical-petrologic classification for the chondritic meteorites. *Geochimica et Cosmochimica Acta, 31,* 747-765.

Wasson, J.T. (1985). *Meteorites: Their record of early solar-system history.* New York, USA: W.H. Freeman and Company.

Wlotzka, F. (1993). A weathering scale for the ordinary chondrites (abstract). *Meteoritics, 28,* 460.

Analysis of Orbital Dynamics in the Gravitational Field of a Rectangular Parallelepiped

Grace Dupuis, University of Victoria (gdupuis@uvic.ca)

Abstract

This study presents an analysis of simulated satellite orbits in the exact gravitational field of a rectangular parallelepiped. In particular, the secular changes of orbital elements are analyzed under varying inclination and aspect ratio. The rates of precession of the ascending node and periapsis were calculated both theoretically, by second-order perturbation theory, and computationally, from orbits integrated in the exact field. It is shown that the results obtained upon integration of the exact field agree strongly with the dependence of the precession rates upon inclination and aspect ratio as predicted by general second-order perturbation equations.

1. Introduction

The analysis of the gravitational two-body problem is in most cases limited by the inability to obtain an exact expression for the potential when one or both bodies are not spherically symmetric. It is established that an orbit about a spherically symmetric body will result in a Keplerian ellipse. However, in the case of a non-spherical object, which includes most asteroids with diameters less than about 400 km, the resulting orbit will be perturbed from the closed elliptical trajectory. The orbit of a small object, such as a satellite, in the gravitational field of an asteroid represents one such instance. As noted by Dawson and Johnson (2007), closed-form expressions may be found for both the gravitational potential and field of a rectangular slab, a shape that proves to be a reasonable approximation to certain asteroids. They examine several orbits in this field and address the applicability of such a hypothetical situation in analyzing actual satellite-asteroid systems such as the Ida-Dactyl system (Figure 1). Moreover, the stability of such systems is analyzed in the continuing study conducted by Brown (2009). Under the suggestions for undergraduate research posed by Dawson and Johnson, the analysis of satellite orbits in this hypothetical field is continued.

The specific case of an oblate symmetric top, in this case a slab with sides $2\alpha = 2\beta \geq 2\gamma$, is examined and orbits of both varying inclination and aspect ratio are compared. In particular, the precession of the line of nodes and the line of apsides is analyzed, both under this exact expression and the general expansion of the potential of an arbitrary body.

2. Perturbation Equations

The expressions for the secular changes of orbital elements are first derived here, as predicted from the expansion for the potential of an arbitrary

body. Consider a body of mass M, and let r denote the distance of an external point, P, from its centre of mass. The Legendre polynomial expansion of the potential at P for a body that is dynamically symmetric about the z-axis, taken to order r^{-3}, is given by Roy (1988) as

$$U = \frac{GM}{r} + \frac{G(C-A)(1-3\sin^2\phi)}{2r^3}, \tag{1}$$

where ϕ is the latitude of the point P, and C and A are the principal moments of inertia of the body. The motion of a particle under the associated perturbing function

$$R = \frac{G(C-A)(1-3\sin^2\phi)}{2r^3}, \tag{2}$$

is now considered. The latitude of the particle is given by $\sin i \sin(\omega + \upsilon)$, where i is the inclination of its orbit, ω is the argument of the periapsis and υ is the true anomaly. Hence, the perturbing function may be expressed in the form

$$R = \frac{G(C-A)(1-3\sin^2 i \sin^2(\omega+\nu))}{2r^3}. \tag{3}$$

Expansion of the time-dependent variables, υ and r, in terms of the mean anomaly yields an expression in terms of the orbital parameters and time. As only the secular variations in the orbital elements are being investigated here, only the constant term is given. Furthermore, assuming orbits of low eccentricity, the expansion is taken to order e^2. The perturbing function then becomes

$$R = \frac{G(C-A)}{2a^3}\left(1+\frac{3}{2}e^2\right)\left(1-\frac{3}{2}\sin^2 i\right), \tag{4}$$

where a is the semi-major axis of the orbit.

The secular variations in the longitude of the ascending node and the argument of periapsis are now explored, under the potential given in equation (4). First consider the precession of the line of nodes. By Lagrange's planetary equations, the rate of precession of the ascending node is given by

$$\dot{\Omega} = \frac{\dot{1}}{\sqrt{GMa(1-e^2)}\sin i}\frac{\partial R}{\partial i}. \tag{5}$$

For the potential in this case, the equation then becomes

$$\dot{\Omega} = -\frac{3}{2}\sqrt{\frac{G}{Ma^7}}(C-A)\frac{(1+\frac{3}{2}e^2)}{\sqrt{1-e^2}}\cos i. \tag{6}$$

Binomial expansion of the above expression to order e^2, yields

$$\dot{\Omega} = -\frac{3}{2}\sqrt{\frac{G}{Ma^7}}(C-A)(1+2e^2)\cos i. \tag{7}$$

In the case of an oblate symmetric top, C – A> 0 and it is evident from equation (7) that the line of nodes will regress, independent of the orbital inclination, with the exception of the extremal cases of $i = \pm 90°$ for which $\dot{\Omega}=0$. Now the predicted behaviour of the line of apsides is examined. The rate of precession of the argument of periapsis is given by Lagrange's equations to be

$$\dot{\omega} = \frac{1}{\sqrt{GMa}}\left(\frac{\sqrt{1-e^2}}{e}\frac{\partial R}{\partial e} - \frac{\cot i}{\sqrt{1-e^2}}\frac{\partial R}{\partial i}\right). \tag{8}$$

Differentiation of the perturbing function gives the exact expression to be

$$\dot{\omega} = \frac{3}{2}\sqrt{\frac{G}{Ma^7}}(C-A)\left(\frac{1}{2}\sqrt{1-e^2}(3\cos^2 i - 1) + \frac{1+\frac{3}{2}e^2}{\sqrt{1-e^2}}\cos^2 i\right). \tag{9}$$

Upon binomial expansion of the expressions involving the eccentricity and neglecting terms of order e^2 or higher, the equation for the rate of change of the argument of periapsis becomes

$$\dot{\omega} = \frac{3}{4}\sqrt{\frac{G}{Ma^7}}(C - A)(5\cos^2 i - 1) \tag{10}$$

It is clear from equation (10) that the direction of precession of the line of apsides is subject to the inclination of the orbit. Under the specified order of approximation, the line of apsides will advance for inclinations less than arccos $\left(\frac{1}{\sqrt{5}}\right)$ = 63°.4 and will regress for greater inclinations.

3. Orbits of Varying Inclination

According to the theoretical first-order equations, derived in the previous section, the rates and directions of precession of both the ascending node and the periapsis are determined by the inclination of the orbit. The dependence of the rates of precession of Ω and ω upon inclination is investigated for orbits in the field of a rectangular slab. Using the expressions obtained by Dawson and Johnson for the components of gravitational acceleration, the equations of motion, given in the Appendix, were integrated for the case of a non-rotating slab. A 15th-order Radau integrator (Everhart 1985) was used to obtain the orbits. Let 2α, 2β, and 2γ denote the dimensions of the slab in the *x, y,* and *z* directions respectively. In accordance with Dawson's and Johnson's convention, the *x, y,* and *z* axes are chosen to coincide with the principal axes of the slab, with $\alpha > \beta > \gamma$. For this particular case, the dimensions were chosen such that $\alpha = \beta = 20$ km and $\gamma = 10$ km and the density, ρ, was chosen to be 2500 kg m^{-3}. The satellite was initially positioned such that $x_0 = r_0$, $y_0 = z_0 = 0$ with initially circular velocity of components $\dot{x}_0 = 0, \dot{y}_0 = \epsilon\sqrt{\frac{\mu}{r_0}}$ and $\dot{z}_0 = \sqrt{\frac{(1-\epsilon^2)\mu}{r_0}}$, where $\epsilon = \cos i_0$ and $\mu = GM_{\text{slab}}$. The following system of dimensionless units was adopted in computing satellite trajectories. Introducing α as the unit of length, velocity, acceleration, and time were expressed in units of $\alpha\sqrt{G\rho}$, Gρ and $\frac{1}{\sqrt{G\rho}}$ respectively. The motion of the satellite was integrated for 4.0×10^3 units of time, equivalent to 1.0×10^7 s, with points taken at times in increments of 0.10. For orbits integrated under these initial conditions, the orbital inclination was observed to remain constant to within 1°.40. The average rates of precession of both the line of apsides and the line of nodes were determined for 23 initial inclinations, ranging from 0° to 90°. Figure 2 shows the trajectories corresponding to initial inclinations of 10° and 70°. Only the first 2.5×10^6 s are shown, for clarity.

The advance or regression of both the line of apsides and the line of nodes with varying inclination was found to agree with the behaviour predicted by the theoretical expressions for the potential of an oblate symmetric top. The line of nodes was observed to regress for all inclinations, while the direction of precession of the line of apsides changed at an inclination of 62°.6. Figure 3 shows the rates of precession of the ascending node and the periapsis, obtained both computationally and from equations (7) and (10). On the assumption that the semi-major axis was constant between orbits, the plotted precession rates were normalized by their respective values at i = 0°. This assumption proved to be reasonable, as the value of r_0 was varied with the initial inclination, such that the value of a remained constant within 0.0203 percent. Although the variations in inclination did result in a more significant range of eccentricity values, the effect was neglected. According to the derived equations, the only dependence on the eccentricity is to second order, affecting only the precession of the line of nodes; as the eccentricities for these particular orbits were of order 10^{-2} or 10^{-3}, the dependence on eccentricity was considered negligible.

4. Rectangular Slabs of Varying Aspect Ratio

The study performed by Dawson and Johnson was restricted to the case of a slab of particular dimensions, α = 20 km, β = 10 km, and γ = 5 km. In this further investigation, the orbits are examined under varying aspect ratios, $\frac{\gamma}{\alpha}$, for the case of a symmetric top. Consider once again the equations derived in section 2 for the theoretical rates of precession of the ascending node and the periapsis. One can see, by the appearance of the principal moments of inertia in both equations (7) and (10), that the precession rates are subject to the dimensions of the slab. In the case here, the principal moments of inertia are

$$C = \frac{2}{3}Ma^2 \tag{11}$$

and

$$A = \frac{1}{3}M(\alpha^2 + \gamma^2)\cdot \tag{12}$$

Writing the rates of precession in terms of the dimensions of the slab then yields

$$\dot{\Omega} = -\frac{1}{2}\sqrt{\frac{GM}{a^7}}(1 + 2e^2)\cos i(\alpha^2 - \gamma^2) \tag{13}$$

and

$$\dot{\omega} = \frac{1}{4}\sqrt{\frac{GM}{a^7}}(5\cos^2 i - 1)(\alpha^2 - \gamma^2). \tag{14}$$

Evidently, the rates of precession are zero for aspect ratios of 0 and 1, corresponding to a flat plate and a cube respectively; it is perhaps less obvious why the rate of precession is zero for a flat plate, but it is clear when it is recognized that this instance represents the limiting case of zero mass. Hence, at a constant inclination, there is a value of $\frac{\gamma}{\alpha}$ for which the rates of precession of both the ascending node and periapsis reach a maximum. For this analysis of precession rate under varying aspect ratio, the parameters of α and the density of the slab, ρ, were fixed to be 20 km and 2500 kg m^{-3}, respectively. Upon introducing α as the unit of length and letting c denote the aspect ratio, the expressions for the precession rates become

$$\dot{\Omega} = -\sqrt{\frac{2G\rho\alpha^7}{\alpha^7}}(1+2e^2)\cos i(c^{\frac{1}{2}} - c^{\frac{5}{2}}) \tag{15}$$

and

$$\dot{\omega} = \frac{1}{2}\sqrt{\frac{2G\rho\alpha^7}{\alpha^7}}(5\cos^2 i - 1)(c^{\frac{1}{2}} - c^{\frac{5}{2}}). \tag{16}$$

Following optimization of the above expressions, with respect to c, one finds that the maximum rates of precession of both the ascending node and periapsis occur for an aspect ratio of c= $\frac{1}{\sqrt{5}}$ 0.447, the respective maximum values being

$$\dot{\Omega}_{max} = \frac{4}{5^{\frac{5}{4}}}\sqrt{\frac{2G\rho\alpha^7}{\alpha^7}}(1+2e^2)\cos i \tag{17}$$

and

$$\dot{\omega}_{max} = \frac{4}{5^{\frac{5}{4}}}\sqrt{\frac{2G\rho\alpha^7}{\alpha^7}}(5\cos^2 i - 1). \tag{18}$$

The dependence of the precession rates on aspect ratio is analyzed here, under the specific gravitational field of a square slab. The precession rates were numerically obtained for motion in the fields of square slabs with aspect ratios varying from zero to one. The equations of motion, as given by Dawson and Johnson (2007), were integrated with initial conditions $x_0=r_0$, $y_0=z_0$ and $\dot{x}_0 = 0, \dot{y}_0 = \epsilon\sqrt{\frac{\mu}{r_0}}$ and $\dot{z}_0 = \sqrt{\frac{(1-\epsilon^2)\mu}{r_0}}$ Under this analysis, the inclination was kept constant at 15°; thus ϵ=cos 15°. In accordance with the conditions in the derivation of equations (15) through (18), the density was fixed at 2500 kg m^{-3} and α was fixed to be 20 km. Moreover, calculations were carried out in the same system of dimensionless units as was used in the previous section. Orbits were integrated for 5.0 × 10^4 units of time, or 1.22 × 10^8 s, with points taken in increments of 0.1, and the average rates of precession were determined over the duration of each orbit. Orbits were obtained for 24 ratios, ranging from zero to one. Figure 4 shows orbits for aspect ratios of 0.25 and 0.75, each displaying motion over the first 2.5 × 10^6 s. The maximum rates of precession of the line of apsides and the line of nodes were observed to occur for an aspect ratio of 0.440, in good agreement with the value predicted earlier. The experimentally determined variation of the rates of precession of the ascending node and periapsis is depicted in Figure 5. The plotted precession rates were normalized by their respective maximum values. Figure 5 also shows the expected rates, predicted by equations (15) and (16), also normalized by equations (17) and (18), respectively. In using equations (15) and (16) to predict the precession rates, it was assumed that the semi-major axis remained constant with varying aspect ratio. As with the analysis under varying inclination, the value of r_0 was varied, and especially, decreased with increasing aspect ratio, such that the value of the semi-major axis remained constant within 0.0120 percent. Furthermore, the eccentricity remained of order 10^{-2}, and as in the previous investigation its observed variation was concluded to have negligible effect on the precession rates.

5. Summary

The study of orbits in the field of a rectangular slab conducted by Dawson and Johnson was continued here, specifically for the case of an oblate symmetric top. Expressions were derived for the precession rates of the ascending node and periapsis, as predicted by application of the planetary equations to the first-order expansion of the generic perturbing potential. Upon integrating the exact expression for the gravitational field of the slab, the numerically obtained precession rates of the line of nodes and the line of apsides were found to agree with those that were predicted. The dependence of the precession rates on both the orbital inclination and the aspect ratio of the slab were analyzed and the general behaviour was observed to agree with the derived expressions in both cases. Particularly, the direction of precession was examined with varying inclination and the observed dependence was found to agree with what was expected. Moreover, the variation in both precession rates was examined under varying aspect ratio, and the ratio resulting in the maximum rates of precession was determined. The study performed here has examined the accuracy of first-order perturbation theory in predicting the variation in orbital parameters. This investigation has obtained orbits by integration of exact equations of motion and examined the correlation between the numerically obtained secular changes in both the longitude of the ascending node and argument of periapsis, and those predicted by second-order perturbation theory.

6. Acknowledgements

The author thanks Dr. Jeremy Tatum for the help and guidance that enabled this project. The study discussed here has been enabled by the Science Undergraduate Research Award, awarded by the Dean of Science, University of Victoria, and by the University of Victoria department of Physics and Astronomy.

7. Appendix

The expressions, as given by Dawson and Johnson, for the gravitational field of a rectangular slab are given as equations 7, 29, and 30 in the research article in the December 2007 Journal, `www.rasc.ca/journal/pdfs/2007-12-hr.pdf`.

The variables α, β, γ, and ρ are as previously defined and, in keeping with Dawson's and Johnson's notation, the term ρ_{ijk} is defined as $\rho_{ijk} \equiv \sqrt{(x \pm \alpha)^2 + (y \pm \beta)^2 + (z \pm \gamma)^2}$, where *i, j,* and *k* denote the signs of the $(x \pm \alpha)$, $(y \pm \beta)$, and $(z \pm \gamma)$ terms, with a value of 1 corresponding to + and a value of 2 corresponding to –. The equations of motion given in equation 22 were integrated to obtain orbits in the field of a non-rotating slab.

$$\ddot{x} = \frac{g_x}{m}$$

$$\ddot{y} = \frac{g_y}{m} \qquad (22)$$

$$\ddot{z} = \frac{g_z}{m}$$

References

Brown, E. (2009). *Canadian Undergraduate Physics Journal, 7,* 2
Dawson, P.C. & Johnson, R.G. (2007). *JRASC, 101,* 6
Everhart, E. (1985). *Proc. 83rd Colloquium IAU, Dynamics of Comets: Their Origin and Evolution, 115,* 185 Reidel: Dordrecht
Everhart, E. (1974). *Celestial Mechanics, 10, 1*
Fitzpatrick, P.M. (1970). *Principles of Celestial Mechanics,* New York and London: Academic Press
Macmillan, W.D. (1958). *The Theory of the Potential,* New York: Dover
Roy, A.E. (1988). *Orbital Motion,* Bristol and Philadelphia: Adam Hilger

Figure 1 — Ida and Dactyl. Image NASA.

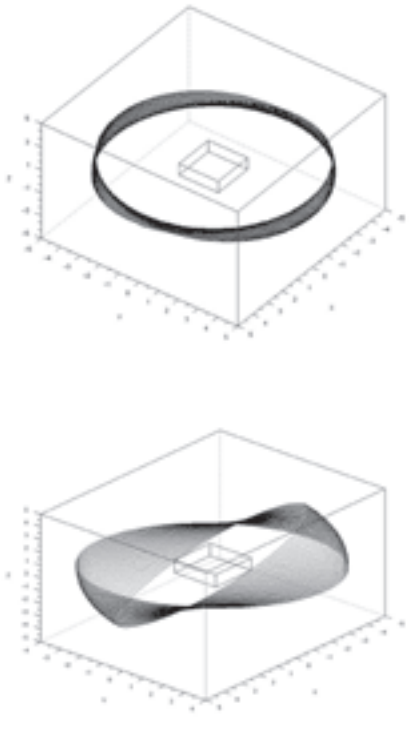

Figure 2 — Figures (a) and (b) show the trajectories for initial orbital inclinations of 10° and 70°, respectively.

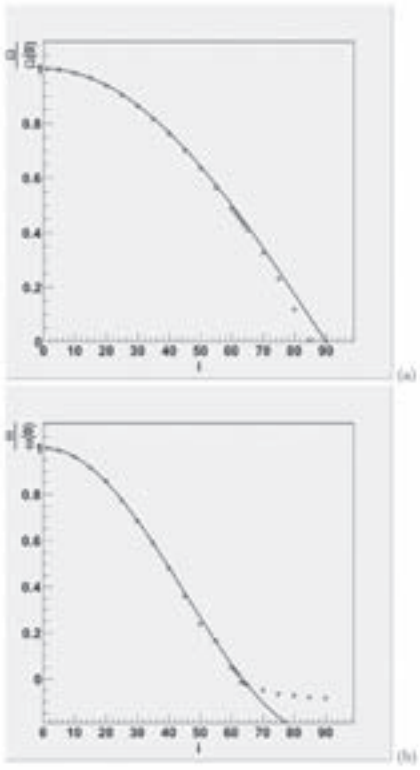

Figure 3 — Figures (a) and (b) show the respective rates of precession of the ascending node and the line of apsides, as a function of the initial orbital inclination. The points show the values obtained from the simulated data, while the expected relations, given by equations 7 and 10, are represented by the solid curves.

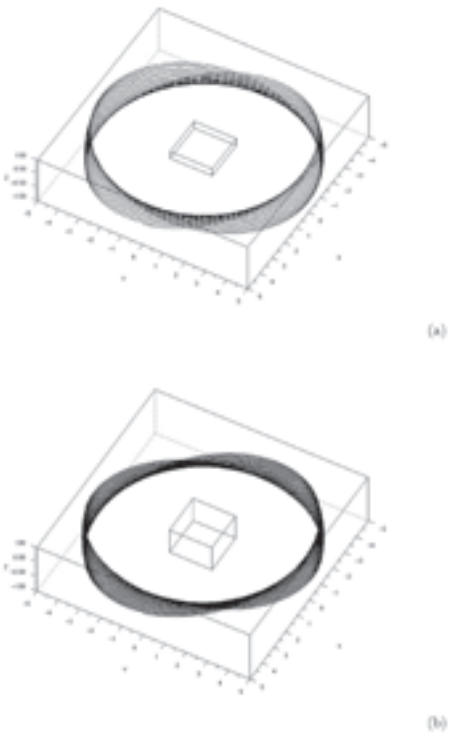

Figure 4 — The trajectories corresponding to aspect ratios of 0.25 and 0.75 are shown in figures (a) and (b), respectively.

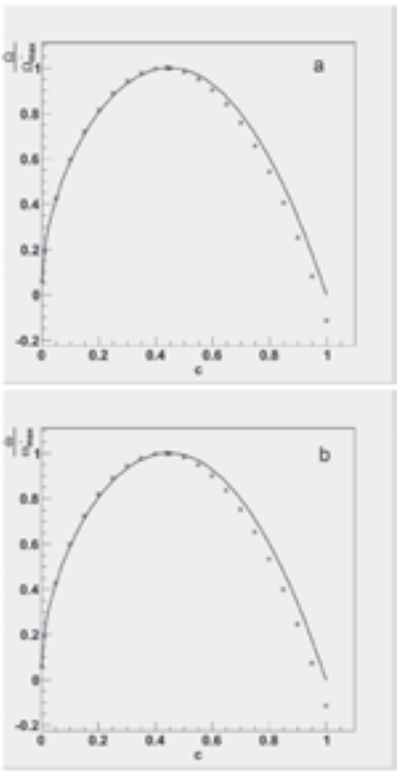

Figure 5 — Figures (a) and (b) show the dependence of the precession of the ascending node and the periapsis on the aspect ratio of the slab. The relations predicted by equations 15 and 16 are represented by the solid curve and the points give the computed results.

Atmospheric Height by Twilight's Glow

by Martin Beech, Campion College, University of Regina

A curse and a joy: these are the feelings brought on by twilight. To the astronomer who is sweeping for comets or searching out those final few Messier objects, the faint glow of dawn in the eastern sky is a curse, heralding the unstoppable on-rush of the Sun and an end to observing. The dawn twilight, in spite of its astronomy-stopping power, is still a beautiful sight to behold — it is indeed the muse of the love-struck poet. Likewise, but in contrast to the on-coming sunrise, the twilight following sunset is a joy for the astronomer since it heralds the onset of observing. Whether marking the end or the beginning of astronomical observing, the twilight phenomena should not be overlooked — there is science and discovery in those diaphanous glows — indeed, they tell us of the atmosphere.

Earth's atmosphere is a mere wisp of gas — a veneer-thin screen that protects us from the deadly ravages of space. Discussed since ancient antiquity, the atmosphere is the quintessential realm of change and material corruption. It is where weather takes place and where the elements of water, wind, and fire are mixed in pouring rain, swirling clouds, snow storms, and lightning: ever changeable, ever quixotic, ever the topic of discussion, and ever interesting. But, what are the physical characteristics of the atmosphere — how high is it and how does it vary with height? While visual observations of twilight phenomena can't provide an answer to the last of these questions, it can offer a guide to the first. Indeed, the answer was first determined in the 10th century by the remarkable Islamic scholar Abu Ali al-hasan ibn al-Hasan ibn al-Haytham (965 - 1039) who is better known through his Latinized name Alhazen. The geometry of the situation is quite straightforward and shown in Figure 1. The idea is that the minimum height of the atmosphere can be determined according to the limit set by solar illumination.

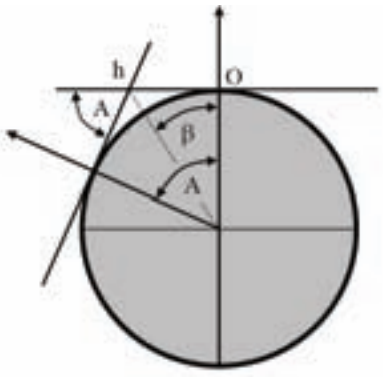

Figure 1 — The geometrical arrangement of Alhazen's twilight problem. The observer is located at point O and the zero-horizon illumination condition is satisfied once the Earth has spun through angle A. The height of the atmosphere is determined at the half angle β = A/2.

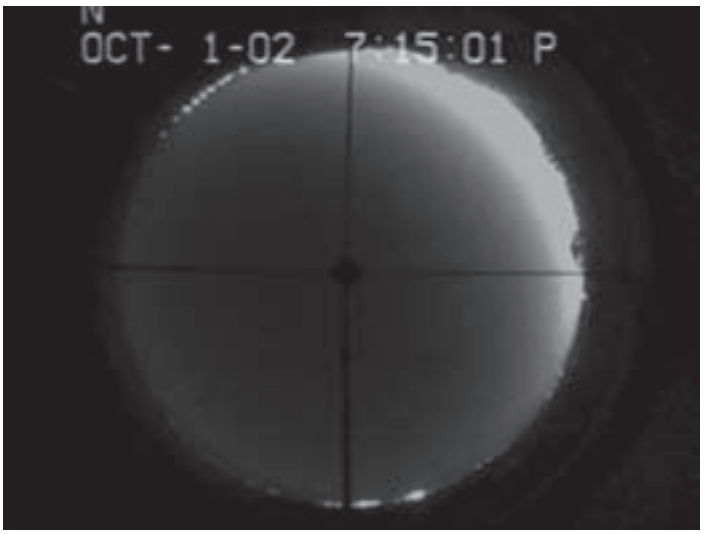

Figure 2 — One of all-sky images from the video sequence recorded on 2002 October 01 from Regina, Saskatchewan. The image is in a negative format and the twilight crescent is clearly visible in the western sky.

The trick is to gauge the angle A (the Sun's elevation below the horizon) at which the atmosphere is no longer appreciably illuminated by sunlight as viewed by the observer at O. Provided an estimate of angle A can be made, then the geometry indicates that the approximate height of the atmosphere is $h = R_E [\sec(\beta) - 1]$, where $\beta = A / 2$, and R_E is the Earth's radius. Alhazen realized that angle A could be estimated by measuring the duration ΔT of the twilight phenomenon — this is the time, for example, between the moment of sunset and the disappearance of the last skyglow on the horizon. Once ΔT has been measured, then the elevation of the Sun (below the horizon, of course) at the onset / or end moment of twilight can be determined. This result follows from the fact that the Sun appears to move through the sky at a rate of 15 degrees per hour. There is just one final twist, and this relates to the fact that in general the Sun does not rise and set along a vertical path with respect to the horizon — in general, the Sun's path will be at an angle $\alpha = 90 - \lambda$ degrees, where λ is the observer's latitude. Spherical trigonometry provides the final result that we want — namely: $\sin(A) = \sin(\alpha) \sin(\Delta T \times 15)$.

Inspired by a recent reading of Alhazen's works, it seemed only appropriate to try to repeat his twilight observations. Being far too old (or is that too wise?), to endure the wonders of a Saskatchewan sunset in the depths of winter (the time at which I was reading over Alhazen's works) I turned to a stock of canned video data collected with an all-sky video camera used primarily to monitor for fireball activity. An old videotape for 2002 October 1 seemed to fit the bill. Data collection on that night began prior to sunset and it was a

glorious cloud-free night. The tape reveals that the sunset occurred at approximately 18:30 local time — perhaps it should be noted here that I had decided before starting the tape analysis to not check the actual sunset time until all the numbers were gathered in. The time of sunset is easily found, of course, with any planetarium program, and as it turned out, sunset was at 18:27 local time. A series of still images was obtained from the video sequence (Figure 2), and from these the height of the twilight crescent in the western sky was measured. In an attempt to determine a good estimate for the time of the last horizon glow, the projected radial distance from the mirror centre (where the image of the video camera itself is located) to the centre of the twilight arc was measured. The results of these measurements are shown in Figure 3. The gradual approach of the twilight arc to the horizon is clearly delineated from approximately 18:45 to 19:45, and, by fitting a smooth curve to the measured data points, the zero-horizon illumination time is predicted to be 19:55. The deduced twilight time interval was found to be ΔT = 75 minutes. With this deduced time interval the Sun's elevation below the horizon at the time of zero-horizon illumination is A = 11.9 degrees.

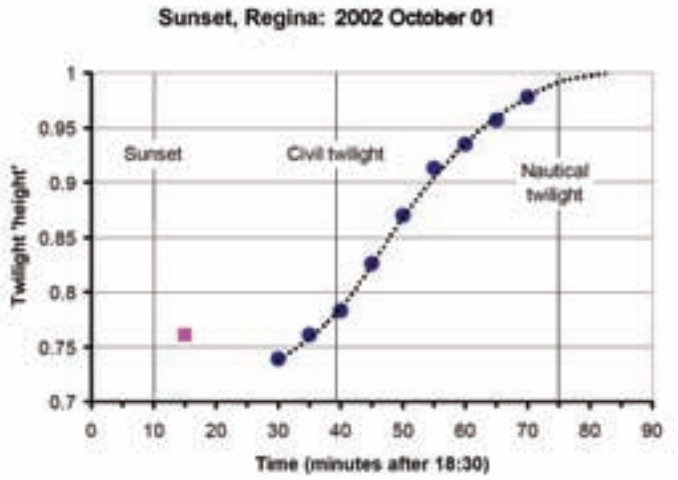

Figure 3 — Analysis of the projected distance from the centre of the mirror to the centre point of the twilight crescent (normalized with respect to the radius of the mirror). The dots correspond to the data points measured after 19:00 local time. The square corresponds to the first twilight arc measurement at 18:45. The vertical lines indicate the official times corresponding to sunset, the beginning of civil twilight, and the end of nautical twilight.

What we have actually determined in this analysis is an estimate for the end of nautical twilight defined as the time interval during which the Sun is between 6 and 12 degrees below the horizon. In practical terms, nautical twilight corresponds to the time during which the horizon becomes indistinguishable from the sky — this, of course, relates back to the pre-GPS days when maritime navigation was based upon being able to make sextant sightings. The interval prior to the onset of nautical twilight is civil twilight, which technically ends when the Sun is 6 degrees below the horizon. Civil twilight, as the name suggests, is inherently a legally set time limit beyond which many jurisdictions require, for example, the use of headlights on automobiles, and at which a daytime crime switches to becoming a nighttime crime. Astronomical twilight is deemed to begin at the end of nautical twilight and corresponds to solar elevations between 12 and 18 degrees. Nighttime is somewhat arbitrarily said to begin once magnitude +6.5 stars (the limit of human vision) become visible (under perfect viewing conditions) in the zenith.

Returning to Alhazen's realization that the duration of twilight can be used to estimate the height of the Earth's atmosphere, we have from the deduced horizon illumination condition that A = 11.9 degrees, and accordingly h = 34.7 km. This is clearly (from a modern perspective) a minimum height for the atmosphere, and with the video equipment we cannot go any further, since it does not detect star-like objects much fainter than magnitude -3. Nonetheless, with this minimum height estimate, the domain encompassing more than 80 percent of the atmosphere's mass has been enclosed, and over this altitude range the density will drop by a factor of order 100 of that recorded at ground level. In terms of the recognized atmospheric zones, an altitude of 35 km falls within the upper to middle region of the stratosphere, which also encompasses the upper region of the ozone layer.

To push the directly measurable height of the atmosphere higher than the twilight minimum just derived, one will have to investigate the heights of noctilucent clouds, meteors, and fireballs, and these will push the limit upwards by a factor of between 2 and 3 — indeed, comparable to that when the Sun's elevation angle A is some 18 degrees below the horizon.

Bibliography

Adam, John. A. (2009). *A Mathematical Nature Walk.* Princeton University Press

Freely, John (2009). *Aladdin's Lamp: How Greek science came to Europe through the Islamic world.* Alfred A. Knopf, New York.

Meinel, Aden and Marjorie (1991). *Sunsets, twilights and evening skies.* Cambridge University Press

Minnaert, M.G.J. (1993). *Light and color in the outdoors.* Springer-Verlag

Things That Go Bump in the Night: First Anniversary

by Jay Anderson, Winnipeg Centre (jander@cc.umanitoba.ca)

Many years ago, when work intruded into astronomy and observing sessions were limited to late evenings that seldom lingered past 1 a.m., I embarked on a night of light photography (is there any other kind?) at La Barriere Park, a small enclave on the southern side of Winnipeg. Saturn was up, Jupiter was rising, and the bright lights of the city behind me were sufficiently out of the way that the sky would allow photography of some of the brighter objects in the Milky Way.

I arrived in the late twilight and set up on a small dirt road that marked the south boundary of the Park. Further to my south, about 100 metres away, was the dike that protects the city from the floodwaters of the Red River, slightly higher than my position. Behind me to the north was the Park itself, a densely treed oasis that blocked some of the city lights. Photography involves a tedious set-up and alignment, so it was quite dark before I was ready to go; by 10:00, my photographic efforts were underway. I was not completely alone — in the park, a van had come in and settled into a spot in the parking lot behind me, while another small car had braved the dirt road along the top of the dike and parked immediately to my south. There was a small amount of traffic on the gravel road east of me, but that road didn't lead to anywhere important, so it was only an occasional headlight that broke the gloom.

It was a quiet night at the start, with little to disturb my activities. Lights came on briefly in the van and the car, but soon went out, leaving me to the night skies and the lingering summer mosquitoes. A quiet half-hour or so passed by, until a car came from the north, crunching along the gravel road past the Park gates, until it was opposite the road (more a path than a road) that harboured my telescope. The car stopped, and then backed up slowly, until it was able to turn into the park. It came up behind the van, stopping about a half-dozen car lengths behind. A red-revolving light was switched on suddenly, and after a pause of about two minutes, two flashlight-carrying policemen exited the squad car and approached the van, shining their lights on its back door in warning. They knocked on the driver's door, a window was rolled down, and there was a brief muffled conversation.

In a few moments, the van came alive, lights were turned on, the engine started, and it left the park, headed back to the city. The police returned to their vehicle, and also left the park, continuing their slow patrol southward along the gravel road. They passed me, but turned at the dike and drove cautiously onto the dirt road toward the car. They didn't go far — only a couple of car lengths — and then proceeded to repeat the routine that had been demonstrated in the parking lot with the van. They had a somewhat longer walk to the parked car, but even then, the lights came on fairly slowly, and one of the occupants of the parked car had to exit the rear seat, presumably to retrieve a bit of identification.

The police returned to their patrol car, backed off the dike, and turned back to the north.

"Well, now it's my turn," I thought, and it was. I removed the camera from the telescope, pointed it at Saturn, put in an eyepiece, and waited.

They were very polite. "What are you doing here?"

"Looking at the stars with my telescope."

"What are you looking at?"

"Saturn."

"Can we have a look?"

And so, for about 10 minutes, I showed them some of the sky. They were quite entranced with the views.

"Can you see into the car on the dike?" one asked.

"No, I don't think so. It's a bit above me on the dike."

"That was the most organized woman I've ever seen" volunteered one of the cops. "She even had a nightgown."

"That was an evening dress" said his companion.

They lingered a few more minutes and then made their departure. "Have a good time," one said, "Everyone else in the park is."

The car on the dike started up immediately after the cops had left. Alas, there was a reason that the police had not travelled along the dike — the car was stuck in the mud. For ten minutes, the driver tried to extricate himself from the muck. Fed up with the noise and the activity, and with deadlines approaching, I packed up and put the mounting and telescope into my Datsun. Ready to leave, I realized that I couldn't just leave the people on the dike to their fate.

"Do you want a ride somewhere?" I shouted across the short field that separated us, to a driver who had exited to inspect the morass around his car.

There was a brief pregnant silence, then "OK."

They trudged along the dirt road, to the highway, where I met them in my car. I had space in the passenger seat, and my Celestron occupied only half of the back seat. She sat in the back, he took the front.

"It's our first anniversary" he offered.

"Congratulations" I replied. "Sorry for the space, but there's no room for my telescope in the trunk."

She said nothing. Ever. The mood was icy cold in the car.

Now most of us understand that a telescope really isn't that good at spying on cars in the dark, but I'm not sure that this couple really made that connection. The guarded attempt at conversation by my passenger was not repeated, and we drove in silence to the nearest open coffee shop. It was midnight by then, and their night was just beginning to get complicated. I left them with my best wishes and a host of discomforting thoughts.

I wonder if there was ever a second anniversary.

Do you have a "Things that go Bump in the Night" story? If so, send it along to editor@rasc.ca. The more embarrassing, the better.

Pen & Pixel

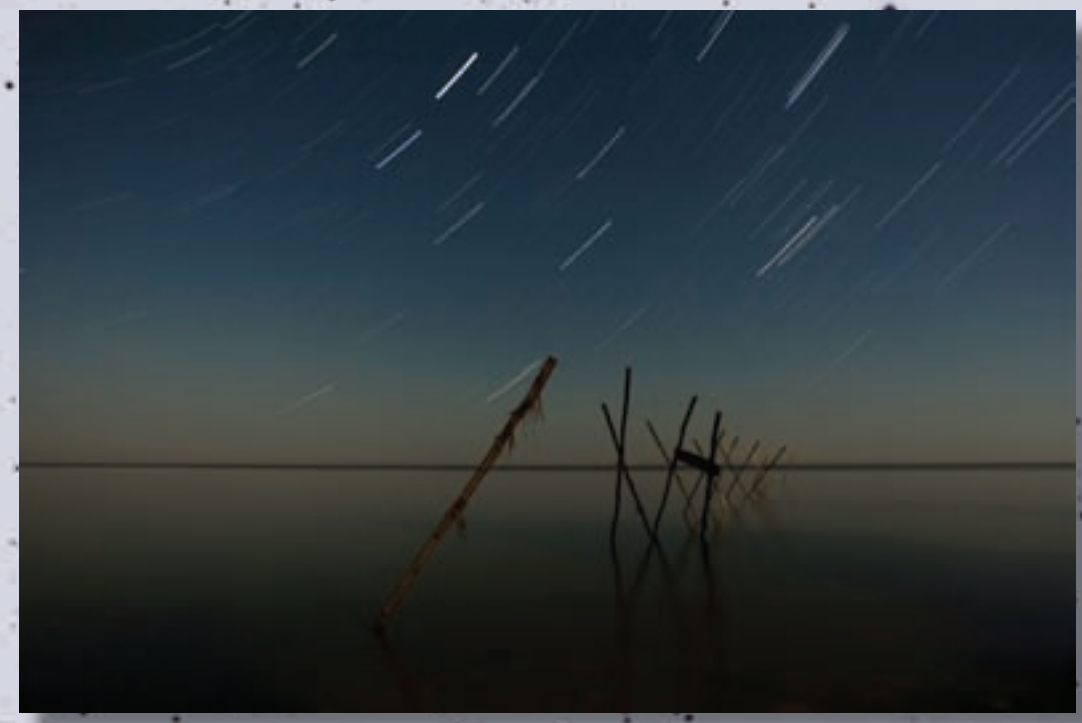

Ron Berard shot this star-trail image over the remnants of the pier at Winnipeg Beach earlier this year. The pier may have been destroyed by spring storms in 2009, but Auriga hangs above its carcass to remind us that the Universe is much more permanent. Ron composed the image from 51 frames exposed for 5 seconds each with a Nikon D70 and a Sigma 14-mm lens set at f/2.8. Individual images were then stacked in *Photoshop* using the lighten-blending mode. Ron used a single flat and no darks.

Comet McNaught put on a fine show low in the north in the early morning hours of June 14 this year. Winnipeg's Kevin Black battled mosquitoes, wood ticks, aurora, fog, and a night that never got truly dark to wrestle this image into his camera from the "Dukes of Hazzard" road east of the city. This 192-second image was acquired using a Canon 20Da at ISO 1600 on a 5.2-inch APO at f/6.

The conjunction of the Moon, Venus, and Mercury on April 15 brought a lot of photographers out that evening. John W. McDonald captured this view on "a beautiful evening at the Victoria Centre Observatory...." Mercury can be found below and slightly right of the Moon, about halfway to the horizon. Exposure was 1.6 seconds at ISO 400 and f/8 using a Canon T1i at 55-mm focal length.

The Toronto Centre's Joel Parkes used a Takahashi 90-mm f/4.5 Sky90 refractor and an SBIG ST8XME from his observatory in Meaford to gather the photons for this image of the nebulae in the Gamma Cygni region. This field is a mosaic of two images composed from a total exposure of 280 minutes in Hα, OIII, and SII filters.

The CASTOR Satellite Survey, 2007 January 1 to 2009 December 31

by Michael A. Earl, Ottawa Centre (mikeearl@castor2.ca)

Introduction

The question is deceptively simple. How many satellites can be detected using only medium-aperture telescopes and CCD cameras? The answer is elusive, since no private individual in Canada (or possibly the world) has actually attempted to find out — until now.

In 2007, the 50th anniversary of the *Sputnik* satellite launch, CASTOR (Canadian Astronomy, Satellite Tracking, and Optical Research) undertook a challenge that began to seriously answer the question. The original challenge was to detect 1957 individual satellites in one year. CASTOR took every single clear night of 2007 to detect as many satellites as it could using a NexStar 11 GPS telescope and an SBIG ST-9XE CCD camera.

At the end of 2007, the CASTOR project had managed to detect a total of 2053 satellites, and yet there were still many that could be detected. In 2009, the International Year of Astronomy, CASTOR embarked on a supplementary project to detect the remaining accessible satellites. This paper describes the IYA campaign and the combined results from both satellite surveys.

The CASTOR Satellite Catalogue

As I began to untangle the massive amount of data from the 50,000 CCD images that CASTOR had amassed in 2007, I decided to organize all of the satellites I had previously detected into a new catalogue. The CASTOR Satellite Catalogue is the listing of satellites that the project has detected since 2007 January 1 in order of detection. When completed, the catalogue will list all of those satellites that can reasonably be detected using medium-aperture telescopes equipped with CCD cameras.

The entire CASTOR Satellite Catalogue is currently available on the CASTOR Web site. Each satellite entry features a link to a sample CASTOR image of the satellite in question for verification purposes.

The first satellite in the catalogue will not be familiar to most readers, but it nevertheless symbolized the beginning of a three-year quest. CASTOR #0001 is the Russian *Cosmos 1674* satellite, first detected on 2007 January 2 from Brockville, Ontario. I have detected this satellite many times since that first day, as well as many of the others that are now in the Catalogue.

The final satellite detected by CASTOR in 2007 (#2053) was another "unfamiliar" Russian satellite named *Cosmos 2146.*

The CASTOR IYA Satellite Survey – Preliminary

On 2009 January 1, CASTOR continued searching for additional satellites to supplement its 2007 catalogue. The challenge was to detect and track an additional 1000 satellites that had not been previously detected in 2007.

Since nobody knew the total number of satellites that could be detected with such equipment, it was unknown at the time whether I could actually detect an additional 1000 satellites during IYA. The 2009 survey was used to find out where CASTOR's "brick wall" was.

The first satellite detected in 2009 was an American *Delta 1* rocket body — the 2054th detected by CASTOR. I had thought that there would be few surprises in the first several months of the campaign as CASTOR concentrated on Low Earth Orbit (LEO) satellites. An event that occurred 788 km over northern Siberia on 2009 February 10 proved me very wrong.

The *Iridium 33 – COSMOS 2251* Satellite Collision

I first heard the news that two satellites had collided from a good friend and fellow Ottawa RASC member. I immediately checked out news reports to confirm one of my greatest fears. Two satellites had collided over Siberia that morning at 11:56 a.m. EST. This was the first collision between two fully intact payloads. One of the satellites was already identified: *Cosmos 2251*. The second was only identified as an *Iridium* satellite, a rather vague statement. I had to use orbit elements from all of the *Iridium* satellites just to identify which of the 77 satellites had collided with *Cosmos 2251*. Finally, I identified the second satellite as *Iridium 33.* 2009 would not be a boring year.

From the day of the collision, I attempted to detect any piece of the collision debris to add to the CASTOR Satellite Catalogue. I used predicted debris orbits from both Iridium 33 and Cosmos 2251, since nobody knew at such an early time whether large or small pieces had been created. I pointed the telescope at the expected location of the debris belts and waited for a detection — any detection. I and CASTOR waited, and waited, and waited.

Finally, on the evening of 2009 March 19, I detected a single piece of what was once *Iridium 33*. I do not know what piece of the satellite I detected on that day. It could have been a piece of a solar panel, high-gain antenna, or even a circuit board (Figure 5c).

Since it was evident that I was just as experienced in satellite collisions as anyone else, *i.e.* no one had any practical experience in the area, I decided to write an ambitious research paper in the midst of the IYA2009 satellite survey. "*The Iridium 33 – Cosmos 2251* Collision: Creating Liability for Space Property and Contemplating the Future of Space Surveillance" eventually reached 42 pages in length. The paper explored the future liability for satellite collisions based on the most recent United Nations legislation on the subject (published in 1972).

The CASTOR IYA Satellite Survey – Satellites Detected

On 2009 December 29, my final clear night of the year, I detected my 1100th satellite of IYA2009. The final three-year tally ballooned to 3153 distinct satellites. The last satellite of 2009 was *Iridium 19,* launched just 13 days after its ill-fated cousin, *Iridium 33*.

This total number is astonishing — and it is still not over. On my final clear night, I was still detecting new satellites. The survey is not yet complete.

The number of orbiting bodies detected each month in 2007 and 2009 is substantial, as illustrated in Figures 1 and 2. However, the 2007 campaign was certainly more labour intensive than the 2009 campaign.

The future of space surveillance (satellite tracking) will ultimately depend on the practical experience of highly dedicated and knowledgeable people who will detect, track, and catalogue satellites on a regular basis. In other words, for satellite tracking to be truly useful, it will have to become an accepted science, not only to military institutions, but also to private users.

The two CASTOR surveys are just the beginning of this endeavour. The first step is to determine the nature of the beast — in other words, how many satellites are we talking about? How is the satellite population distributed? How many from each orbit type can be detected by optical means? How accurately can each satellite be tracked? What is the accuracy of the derived orbital elements?

Name	Type	Orbit	Owner	No. Detected	Total No.	% Detected
AMC	P/L	GEO	USA	15	18	83
ANIK	P/L	GEO	CANADA	15	15	100
ARIANE 5	R/B	VAR	FRANCE	24	41	59
ATLAS 2A	R/B	VAR	USA	12	14	86
ATLAS CENTAUR	R/B	VAR	USA	49	60	82
BLOCK DM-SL	R/B	MEO	SEA	23	26	88
BREEZE-M	R/B	VAR	RUSSIA	27	34	79
BREEZE-M TANK	DEB	VAR	RUSSIA	31	33	94
COSMOS	P/L	VAR	RUSSIA	526	1089	48
DELTA 1	R/B	VAR	USA	41	76	54
DELTA 2	R/B	VAR	USA	31	61	51
DIRECTV	P/L	GEO	USA	12	13	92
ECHOSTAR	P/L	GEO	USA	11	11	100
EKRAN	P/L	GEO	RUSSIA	11	21	52
GALAXY	P/L	GEO	USA	26	28	93
GLOBALSTAR	P/L	LEO	GS	60	60	100
GLONASS GPS	P/L	MEO	RUSSIA	107	112	96
GOES	P/L	GEO	USA	13	15	87
GORIZONT	P/L	GEO	RUSSIA	23	33	70
INTELSAT	P/L	GEO	INTELSAT	43	80	54
IRIDIUM	P/L	LEO	USA	80	90	89
METEOR	P/L	LEO	RUSSIA	44	51	86
MOLNIYA	P/L	MEO	RUSSIA	53	53	100
NAVSTAR GPS	P/L	MEO	USA	50	58	86
ORBCOMM	P/L	LEO	ORBCOMM	28	42	67
SATCOM	P/L	GEO	USA	11	13	85
SL-3	R/B	LEO	RUSSIA	44	58	76
SL-6	R/B	MEO	RUSSIA	112	118	95
SL-8	R/B	LEO	RUSSIA	226	298	76
SL-12	R/B	VAR	RUSSIA	223	270	83
SL-14	R/B	LEO	RUSSIA	102	110	93
SL-16	R/B	LEO	RUSSIA	22	22	100

Table 1: The most detectable satellite types as determined by CASTOR. P/L = Payload; R/B = Rocket Body; DEB = Debris; LEO = Low Earth Orbit; MEO = Mid Earth Orbit; GEO = Geosynchronous Orbit; HEO = High Earth Orbit; VAR = Variable Orbit Altitude; TOTAL No. = Total Number of Type in Orbit; % Detected = Percentage of satellite type in orbit detected by CASTOR.

Orbit Type	Average Altitude	Detected	Total in Orbit	% of Total
LEO	< 1,700 km	1,525	11,015	13.8
MEO	1,700 — 35,500 km	937	2,049	45.7
GEO	35,500 — 36,500 km	670	1,017	65.9
HEO	> 36,500 km	21	28	75.0

Table 2 — The total number of LEO, MEO, GEO, and HEO satellites detected by CASTOR from 2007 January 1 to 2009 December 31.

Object Type	Detected	Total Orbiting	% of Total in Orbit	% of Total Detected
Payload	1,713	3,428	50.0	54.3
Rocket Body	1,204	1,859	64.8	38.2
Debris	146	10,216	1.4	4.6
Unknown	90	—	—	2.9

Table 3 — The total number of payloads, rocket bodies, debris, and unknown satellites detected by CASTOR from 2007 January 1 to 2009 December 31.

Arab Satcom (5)	Europe (31)	Intelsat (39)	New ICO (1)	Spain (8)
Argentina (6)	Eutelsat (12)	International (3)	Norway (1)	Sweden (6)
Asiasat (1)	France (117)	Israel (3)	Orbcomm (26)	Thailand (1)
Australia (5)	Germany (14)	Italy (9)	Philippines (1)	Turkey (2)
Brazil (8)	Globalstar (60)	Japan (74)	P. R. China (91)	United Arab Emirates (1)
Canada (29)	Greece (1)	Luxembourg (2)	Russia (1,554)	United Kingdom (9)
Czech Rep. (1)	India (28)	Mexico (6)	Saudi Arabia (3)	USA (854)
Egypt (2)	Indonesia (5)	NATO (4)	Sea Launch (23)	Unknown (90)
ESA (6)	Inmarsat (5)	Netherlands (2)	South Korea (3)	Venezuela (1)

Table 4 — During the CASTOR satellite surveys, satellites from 44 distinct owners were detected. The number of satellites from each owner is indicated in parenthesis.

Finally, how accurate are the satellite ephemerides generated by the orbital elements?

Since the full capability of the CASTOR survey has not been reached, only the first few questions can be partially answered.

CASTOR Satellite Survey Statistics

During the IYA satellite tracking campaign, it became evident that reliable statistics had been collected on the most detectable types of satellites. Table 1 lists the satellite types that CASTOR captured with a minimum threshold of 10 satellites of a specific type. This table represents two-thirds of all satellites in the entire catalogue. Note that the only debris in this list is the *Breeze-M* rocket supplementary fuel tanks. The rest are either payloads or rocket bodies.

The total amount of satellite debris detected seems very small as compared to the total amount of debris that is currently orbiting the Earth. A significant portion of this debris can be directly attributed to the *Fengyun 1C* destruction and the *Iridium 33 / Cosmos 2251* collision. In most cases, debris is much smaller in size than payload and rocket counterparts, especially when it is formed by collision. Every satellite-tracking facility has a technical detection limit; some objects are so small that not even NORAD can detect them. Part of the reason why these two surveys were conducted was to find CASTOR's technical-detection limit.

The CASTOR IYA Satellite Survey – Notable Satellites

Among the 1100 satellites detected in 2009, I was especially pleased to have detected the following:

RadarSat 2 (CASTOR #2074; NORAD #32382): Canada's second radar Earth-observation satellite;

Iridium 33 Debris (CASTOR #2239; NORAD #34078): The only piece of debris CASTOR detected from the Iridium 33 — Cosmos 2251 collision (see Figure 5c);

CTS (*Communications Technology Satellite; Hermes;* CASTOR #2286; NORAD #08585): The world's first direct-to-home broadcast satellite; manufactured in Canada;

Integral (*International Gamma Ray Astrophysics Laboratory;* CASTOR #2327; NORAD #27540): The European Space Agency's high-orbit gamma-ray observatory;

Giove-B (*Jupiter-B;* CASTOR #2336; NORAD #32781): The second of the European Space Agency's new GPS satellites (see Figure 12);

XMM / Newton (*X-Ray Multi-Mirror;* CASTOR #2395; NORAD #25989): The largest of the European Space Agency's space-based X-ray telescopes;

Terra (*EOS AM-1;* CASTOR #2554; NORAD #25994): A multinational NASA scientific research satellite devoted to monitoring the Earth's environment;

Hipparcos (*High Precision Parallax Collecting Satellite;* CASTOR #2708; NORAD #20169): ESA's space experiment devoted to high-accuracy astrometry and proper-motion surveys;

Alouette 1 (*S-27;* CASTOR #3031; NORAD #00424): Canada's first satellite, launched in 1962 (see Figure 7); and

Celestis 3 (CASTOR #3035; NORAD #26034): The "Millennial Flight" of the *Celestis* memorial spacecraft, containing the cremated remains of 33 people.

The CASTOR IYA Satellite Survey – Images

Observations and Conclusions to Date

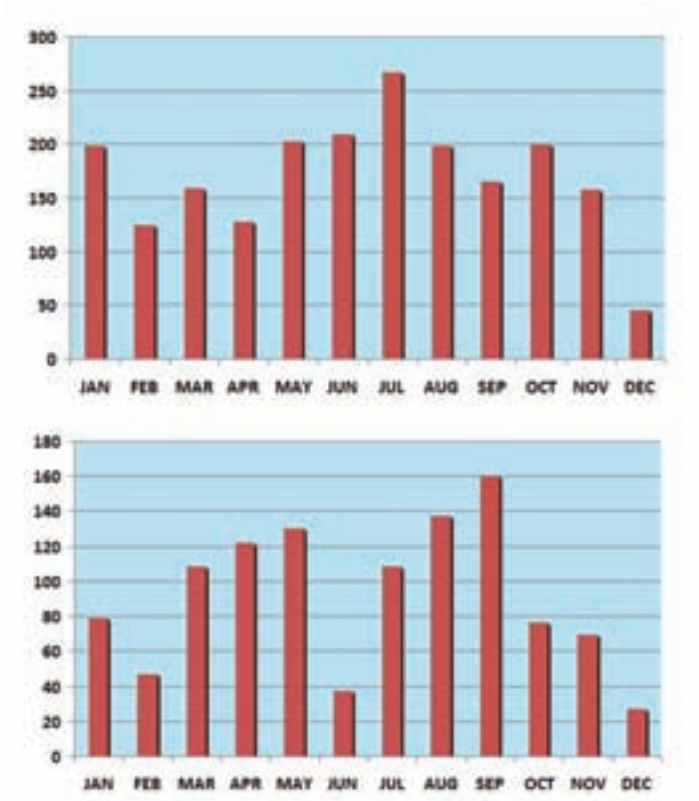

Figure 1 — The number of unique CASTOR satellite detections per month in 2007 (top) and 2009 (bottom).

The CASTOR satellite survey represents the first large-scale optical satellite survey conducted in Canada. No other institution in Canada has attempted or accomplished a satellite survey on the scale done by CASTOR in 2007 and 2009. Although the answer to the fundamental question remains elusive, valuable data has been collected on the brightness, visibility, tumble periods, and orbits of these many man-made objects. CASTOR has shown that a ground-based medium-aperture optical satellite-tracking facility can detect and track over one-fifth of the known NORAD satellite catalogue. This includes nearly one-seventh of all LEO satellites, nearly half of all MEO satellites, about two-thirds of all GEO satellites, and three-quarters of all HEO satellites in orbit.

CASTOR has successfully detected half of all payloads and nearly two-thirds of all rockets currently orbiting the Earth. The statistics can only get better.

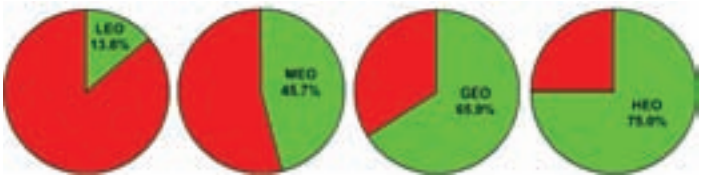

Figure 2 — The percentage of the total number of LEO, MEO, GEO and HEO satellites detected by CASTOR from 2007 January 1 to 2009 December 31.

CASTOR also disproved the belief that ground-based optical satellite tracking facilities would be hampered by light pollution. In fact, most of the satellites CASTOR has detected and tracked were detected in Brockville, which is certainly not light-pollution free. However, detection of debris has proven to be a weak point; in order to detect and track such objects, CASTOR would need to be moved to a darker location.

Debris from the *Iridium 33 / Cosmos 2251* collision as well as debris from the intentional destruction of the Chinese *Fengyun 1C* weather satellite has increased the total number of orbiting objects

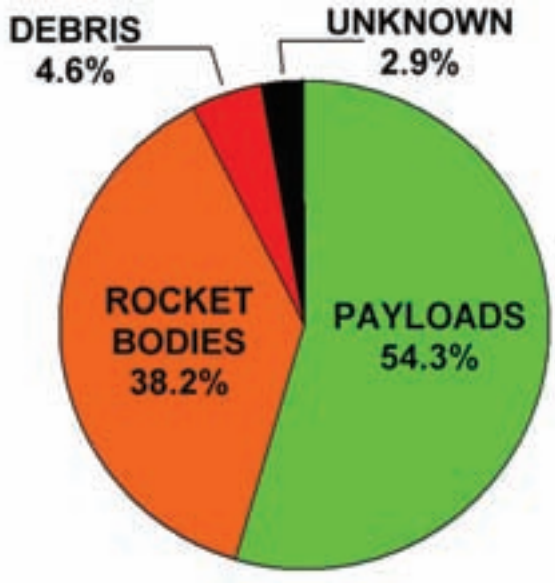

Figure 3 — The payloads, rockets, debris, and unknown satellites detected as a percentage of the total number of satellites (3153) that CASTOR has detected from 2007 January 1 to 2009 December 31.

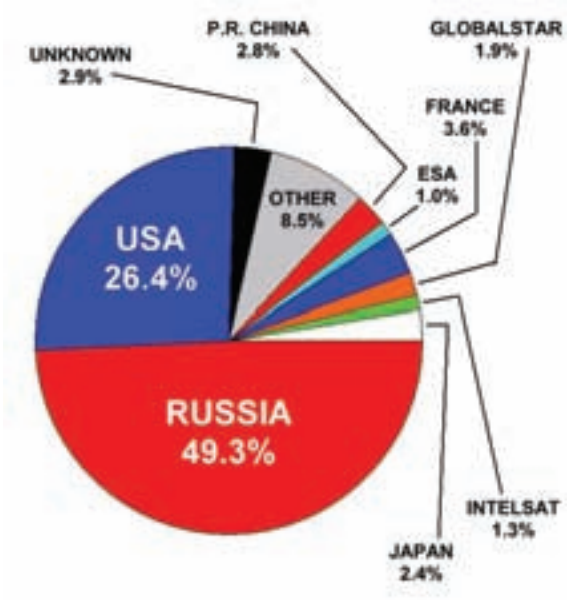

Figure 4 — Ownership of the satellites as a percent of the total number detected. Only those that constitute one percent or more of the total detected are included in the chart.

by approximately 4000. The CASTOR project has detected only three pieces of this debris; two from *Fengyun 1C* and one from the collision. It seems that this is most likely due to the small size of the debris and would explain the small percentage of debris detected during the survey.

The size of a satellite is the only factor that controls its apparent brightness. An observer has to consider the distance, reflectivity, phase angle (sun angle), and orientation (attitude) to anticipate the best opportunity to detect the object. In many cases, CASTOR has had to rely on guesswork about reflectivity, orientation, and size (especially for debris) to plan the search for new satellites.

This project has shown that a low-cost ground-based optical satellite-tracking facility can be used to study the satellite population and provide an excellent education for space-science students. Satellite tracking may become an important activity within the remainder of the 21st century as new methods are investigated to prevent collisions between satellites.

Since 2007 January 1, only 37 satellites in the CASTOR Satellite Catalogue have decayed and fallen back to the Earth. An additional 41 are in advanced orbital decay and will most likely burn up in 2010 or 2011.

The *Iridium 33* / *Cosmos 2251* collision was a significant event in the history of satellite science — one that was completely unexpected. The collision gives a significant warning to all who design, construct, launch, track, and use satellites. Our orbiting infrastructure is more fragile than we are aware; one unfortunate collision can (and eventually will) destroy billions of dollars of invested hardware. Satellite collisions could cost billions more in lost revenue, as affected satellite users search for alternatives. We can choose to develop pre-emptive plans now or pay later, when satellites collide more frequently. At the present time, private industry might not suspect that tracking inactive satellites is a significant return on investment, but given more collisions and damage, it certainly may in the future.

Currently, the future of the satellite population, space law, and space surveillance is uncertain. With dedicated work, ongoing surveillance, and sufficient resources, our satellite population can be made collision-free.

CASTOR is a very small piece of the present, but it is the first serious non-military research endeavour in Canada that attempts to detect and catalogue all satellites in all major orbit types that are accessible to inexpensive ground-based commercial off-the-shelf (COTS) optical equipment.

The Future

CASTOR will continue to detect and track new satellites in 2010 in order to finally answer the question asked at the beginning of 2007. Although new satellites are launched every few weeks, the CASTOR detection rate is normally much higher than the launch rate. The project will continue to analyze photometric and astrometric data for each satellite detected in order to compile the first complete tumble period, brightness, and orbit-data catalogue for those satellites detectable by medium-aperture optical equipment.

CASTOR BIOGRAPHY

Canadian Astronomy, Satellite Tracking and Optical Research (CASTOR) was founded in 2007 to investigate the feasibility of utilizing privately owned and operated ground-based medium-aperture telescopes and CCD cameras to detect and track a significant portion of the satellite population.

CASTOR was founded by Michael A. Earl, who has been heavily involved in satellite tracking since May 1997. He designed, tested, and operated Canada's first remotely controlled and automated optical satellite-tracking facility. CASTOR was founded to continue independent research of the satellite population. The CASTOR Web site can be visited at `www.castor2.ca`.

In the International Year of Astronomy, CASTOR teamed up with the Mississippi Valley Conservation Authority to found Night Sky Conservation (NSC), a program designed to educate the public about the causes and effects of light pollution, and what could be lost if light pollution were allowed to continue unabated. The program features methods of reducing light pollution within neighbourhoods. The official NSC web site can be visited at `www.castor2.ca/nsc`.

Resources

The CASTOR Satellite Catalogue: `www.castor2.ca/13_Catalogue`
Space Track — The Source for Space Surveillance Data: `www.space-track.org`
Chris Peat's Heavens Above: `www.heavens-above.com`
Mike McCants' Satellite-tracking Web Site: `www.io.com/~mmccants`.

Acknowledgements

A special note of thanks goes to General Kevin P. Chilton, Commander of the United States Strategic Command, for his persistent vigilance in the realm of space surveillance.

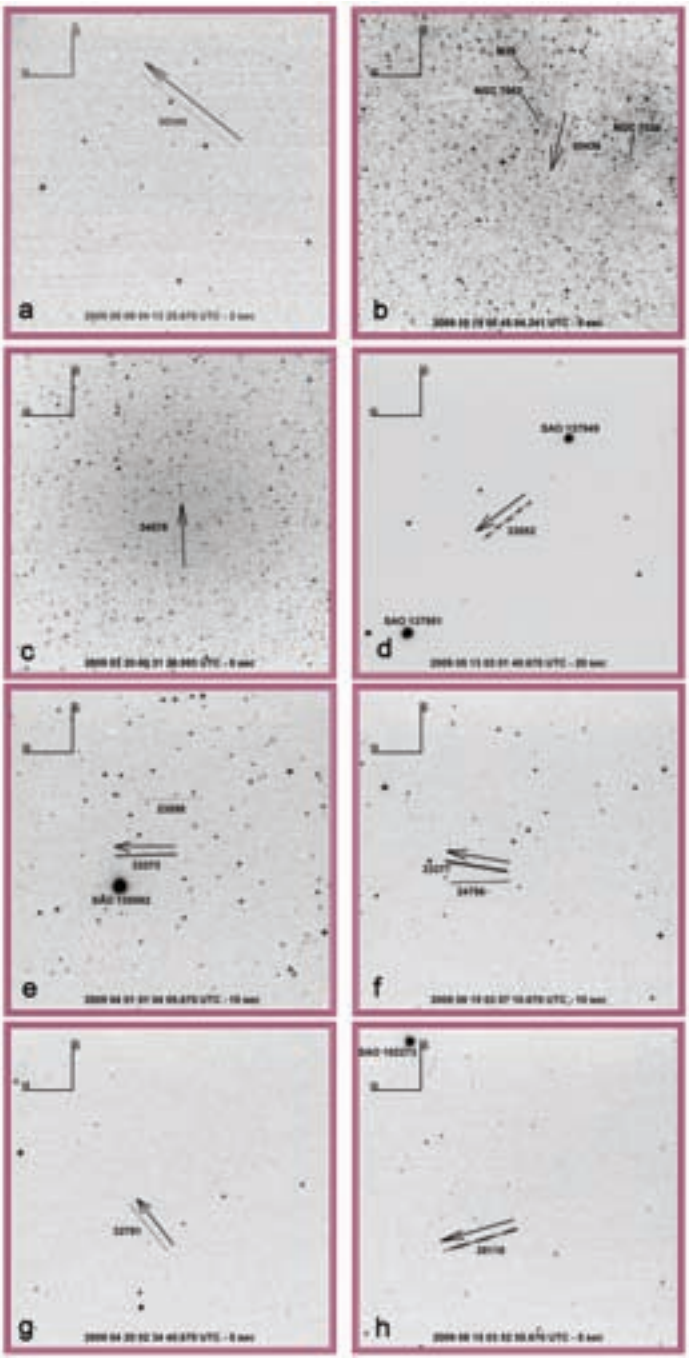

Figure 5 (left) — A sample of satellite images taken as a part of the CASTOR project:

a: *Telstar 1* (CASTOR #0466; NORAD #00340). Although first detected in March 2007, CASTOR continued to track it in 2009.
b: Canada's first satellite: *Alouette 1* (CASTOR #3031; NORAD #00424).
c: An image of a single piece of *Iridium 33* debris from the *Iridium 33 — Cosmos 2251* collision. This might be the only image of the debris ever obtained from Canada.
d: An image of a tumbling *Chinese CZ-3B* (Long March) rocket body (CASTOR #2442; NORAD #33052). Its tumble period was measured to be 4.16 seconds on 2009 May 12.
e: A CASTOR image of the Canadian geosynchronous satellite *Nimiq 4* (CASTOR #2272; NORAD #33373). Appearing just north of it is the co-located satellite *DirecTV 3*, also known as *Nimiq 3* (CASTOR #0841; NORAD #23598). Both satellites are owned and operated by Telesat Canada.
f: An image of a geostationary transfer-orbit rocket body called Block DM-SL (CASTOR #2737; NORAD #33377), originally launched by the Sea Launch company. Just south of it is the *GOES 10* weather satellite (CASTOR #0825; NORAD #24786).
g: An image of the European GPS satellite *Giove-B* (CASTOR #2336; NORAD #32781).
h: A CASTOR image of a tumbling American *Atlas 3B Centaur* rocket body (CASTOR #2743; NORAD #28118).

Dedication

This research paper is dedicated to physicists Dr. Willard S. Boyle and Dr. George E. Smith for their groundbreaking invention of the charge-coupled device (CCD) that made satellite tracking accessible to everyone, and which allowed CASTOR to conduct its research.

Michael A. Earl has been an avid amateur astronomer for over 30 years, and served the Ottawa Centre as both its Meeting Chair and its Vice-President. He constructed the Canadian Automated Small Telescope for Orbital Research (CASTOR) *— the first remotely controlled and automated optical satellite-tracking facility in Canada.*

Period Measurements of Variable Stars Using AAVSO Data

Cody Friesen
University of Manitoba
umfri347@cc.umanitoba.ca

Jennifer West
University of Manitoba
westjl@cc.umanitoba.ca

Abstract: We used the publicly available dataset provided by the American Association of Variable Star Observers (AAVSO) to determine the period of a sample of periodic stars. A discrete Fourier Transform was used to analyze an unmoderated set of observations from this database. Period determinations were made by looking for peaks in the power spectrum of the resulting function. It was found that this method produced values that agreed very well with professional determinations.

Background

Variable stars are stars that vary in brightness over time. This can be caused by a variety of effects. If a star has a binary partner and they orbit one another along our line of sight, we will see the star dim when its neighbour eclipses our view. These are known as extrinsic variable stars. There are also intrinsic variable stars that are caused by changes within the star itself. An example of this is a star that is periodically collapsing. As it collapses, the pressure and temperature inside the star increase, causing more light to be emitted. The increasing pressure then causes the star to expand outwards, restarting the cycle.

Depending on the cause of the variability, observations of the period (the time elapsed between instances of peak brightness) can tell us different things about the star. With extrinsic variable stars, we can determine the masses of the orbiting pairs and details about their orbits. For an intrinsic variable star, we can determine the density of the star and gain insights into its internal structure and dynamics.

Variable stars can also be grouped based on their periods, generally named after a prototype star that is the standard example for that period range. For example, the Cepheids are named after delta Cephei, with periods ranging from a few days to months. There are also Mira variables, named after the star Mira (Omicron Ceti). These stars have much longer periods than the Cepheids, on the order of hundreds of days (Birney 2006).

For many variable stars, quick visual measurements are easy to perform — indeed, it is this lack of the need for complex equipment that makes variable stars a popular topic of study. Precise measurements can be made with a standard camera or dedicated equipment, but magnitude estimates can be made by any observer with a clear sky and a few minutes to spare.

For visual measurements, it is generally required that the target star have one or more nearby comparison stars to provide some convenient scale for comparison. For example, with two comparison stars, the observer can estimate whether the variable star is closer in brightness to one or the other of the stars. For intermediate cases, a linear scale could be used. One method is a scale of 1 to 10, with 1 being the brightness of the first comparison star, proceeding in equal steps up to 10, the brightness of the second comparison star. These measurements can be converted to actual magnitudes using known comparison values at a later time.

Using this method, we observed the variable star Delta Cephei over a period of four months. Delta Cephei is a convenient star to observe visually because is has two nearby comparison stars, Epsilon and Zeta, that have magnitudes closely corresponding to the range of variability of Delta (see Figure 1 for a finder chart). The stars are bright enough to observe visually, even in relatively light-polluted skies and the change in magnitude is great enough to be noticeable over a short period. Our results are shown in Table 1.

Figure 1 — Delta Cephei Finder Chart

Theory

After collecting these visual observations, we became interested in methods of determining the period of a variable star using other data similar to ours. The American Association of Variable Star Observers (the AAVSO) maintains a large database of observations of variable stars. According to their Web site, this database contains over 18 million measurements going back 90 years and is the largest database of its kind in the world. Observations can be submitted by any interested party and are also freely available to anyone for download (AAVSO 2010). We made use of this excellent resource for our analysis. Because anyone can contribute observations, the AAVSO database has become a repository of an enormous amount of data. Unfortunately, this also means that the quality of each observation is not well known. Another disadvantage comes in the unequally spaced nature of the magnitude estimates. For example, in Figure 2 we see a plot of the observations submitted for Delta Cephei.

Table 1: Visual estimates of the brightness of Delta Cephei.

Calendar Date (Starting Night)	Julian Date	UT	Magnitude	Error
2009 September 17	2455092.6	2009 September 18 at 02:25:00	3.5	0.1
2009 September 24	2455099.57	2009 September 25 at 01:45:00	3.4	0.1
2009 September 29	2455104.56	2009 September 30 at 01:25:00	4.1	0.1
2009 October 8	2455113.59	2009 October 9 at 02:15:00	4	0.1
2009 October 13	2455118.57	2009 October 14 at 01:35:00	3.8	0.1
2009 October 22	2455127.53	2009 October 23 at 00:50:00	3.5	0.1
2009 November 5	2455141.65	2009 November 6 at 03:40:00	3.4	0.1
2009 November 7	2455143.57	2009 November 8 at 01:35:00	4.1	0.1
2009 November 17	2455153.56	2009 November 18 at 01:20:00	3.8	0.1
2009 November 17	2455153.64	2009 November 18 at 03:25:00	3.7	0.1
2009 November 19	2455155.58	2009 November 20 at 01:50:00	4	0.1
2009 November 19	2455155.68	2009 November 20 at 04:20:00	4	0.1
2010 January 28	2455225.63	2010 January 29 at 03:05:00	4	0.1

Needless to say, making an accurate measurement of the period from such a plot is very difficult. To extract information, we turn to the methods of Fourier analysis. A Fourier transform is a mathematical technique that decomposes a function into a sum of simpler sine and cosine functions of varying frequency and amplitude. The Fourier transform tells us "how much" of each of the simple functions our original function contains. A periodic variable star should contain a lot of information at one particular frequency (the frequency that corresponds to its period), and so a Fourier transform should be able to identify the dominant period in the signal of a variable star where our eye cannot. Using complex-number notation, this operation can be defined as in Equation 1, with T being the period of the star (Boas 2006).

Equation 1:

$$G(\omega) = \int_{-\infty}^{\infty} F(t) e^{-i\omega t}\, dt$$

$$\omega = \frac{2\pi}{T}$$

In general, this is not a trivial equation to evaluate. But, if our function F(t) is a collection of individual observations instead of a continuous line, we can instead use the discrete form of the transform, as in Equation 2:

Equation 2:

$$G(\omega) = \sum_{t_1}^{t_2} M(t) e^{-i\omega t}$$

Here t_1 and t_2 are the start and end dates of our data, and M(t) is the measurement found for a particular date. In this form, we avoid having to integrate any functions. Our transform becomes a sequence of addition and multiplication operations that give us a coefficient for any individual frequency. Frequencies with higher values correspond to more prominent frequencies in the original data function. We expect that the actual period of the star will result in a clearly distinguishable spike in the power of a particular frequency. Thus, with some foreknowledge of the expected range of the period, we have a method of discovering the true period of the star. This lends itself well to a programming solution, which we discuss later.

Before we can apply this result, we need to process our data into an acceptable form. In this processed form, it must conform to what are known as the Dirichlet conditions in order for the transform to have meaning. There are four conditions in total, but we are mainly interested in the condition that there needs to be a "finite number of discontinuities over the span of the function" (Boas 2006). Stated another way, there cannot be any gaps in our data with respect to time.

To achieve this we define some basic rules for filtering the data. First, a bin size was selected. In this case, a bin is a span of time in which we take the arithmetic average of all of the measurements made during that time and set that as the measurement. For example, we could choose a bin size of one day. It happens that ten measurements were made during a particular day. We would take the average of all of those measurements and set that result as the one measurement for that day.

After our first rule is defined and the data binned, we are left with empty bins. These are common in the unevenly spaced data we used. Any empty bins at the beginning or end of our data were dropped, as no reasonable approximation can be made for their values. For empty bins that lie inside our data we can approximate their values by linear interpolation between the bounding bins. We accomplish this by finding the slope of the line connecting the bounding-bin measurements and finding its value at the midpoint of the empty bin.

If we have multiple empty bins, this method can be extended to cover them all, but we must remember that this is only an approximation. We know that our data is fluctuating periodically — in other words, a curved (non-linear) function. Estimating this change

with straight lines is acceptable over short jumps, but if a particular dataset requires too many of these approximations, our results could become unreliable.

After the data is processed, all that remains is to choose the frequencies we want to examine. For our solution, we specify a range of frequencies and the resolution over that range (the number of evenly spaced frequencies within the range). The results of the calculation are then plotted and may be visually or analytically examined.

Method

Our first approach was to use a spreadsheet program to perform our Fourier Transform. While awkward to set up, it had the advantage of quickly yielding results. A small script was written in *Basic* that built up our list of coefficients and plotted the result. The range of frequencies could easily be changed, but the resolution was not easy to modify. Overall, the spreadsheet allowed us to quickly test our approach and get some preliminary feedback. While a dedicated program was eventually written to do the processing, it should be noted that in principle all of our analysis could have been performed with free spreadsheet software.

For our second approach, a processing program was created using the *Java* programming language. The program is able to parse data directly downloaded from the AAVSO site, perform binning and interpolation operations, and output a list of the desired coefficients and frequencies. Analyzing data becomes a matter of selecting the desired frequency range and resolution, and plotting the results.

The program was implemented in such a way as to allow the individual algorithms involved to be changed separately. The usual approach is to implement a Fast Fourier Transform algorithm of some type, a likely candidate for future upgrades.

Data and Results

To illustrate our analysis technique, we will examine the star Delta Cephei. The AAVSO dataset for this popular star is quite large, containing around 35,000 observations. Because this star is a Cepheid variable, we will start by expanding over the period range of 0.5 to 10 days — a range that encompasses most of the known periods for this type of star. A bin size of 0.5 days was initially chosen to give a reasonable approximation of the changing brightness. This bin size worked well for both Cepheids and Mira-type variables. Shorter-period stars would require smaller bin sizes, as we cannot have too much of the variation occur within a single bin. Finding the right settings for these values requires some experimentation and foreknowledge of the expected period of the star. Once plotted, the expansion takes the form of Figure 3.

First, we note the large spikes present at the lower range of the period. These are a combination of two things: "noise" in the data and artefacts from the transform. Small errors in measurement show up in the frequency analysis as high-frequency components of the data. The spike in coefficients at the shorter-period end of the plot also coincides with our chosen bin size. This occurs at whatever bin size is chosen and is a result of the assumptions we made when processing our data into a function.

Having accounted for the large peaks, we notice a smaller peak in the region of 5.5 days. We can expand around this point. In this case, we found the same number of coefficients but over a smaller range. Plotting our results gives us Figure 4.

Figure 2 — Delta Cephei Magnitude Measurements versus Time

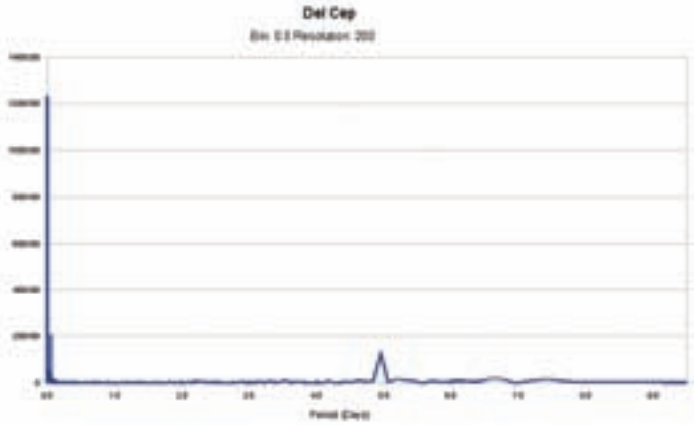

Figure 3 — Delta Cephei First Expansion

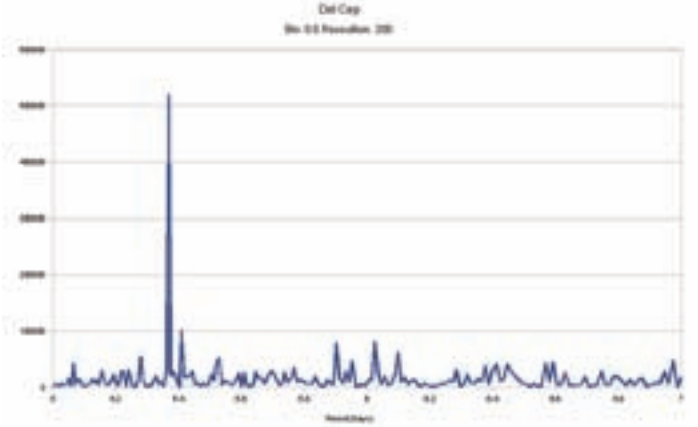

Figure 4 — Delta Cephei Second Expansion

With this expansion, the period becomes obvious. Examining our coefficients, we find that the highest value corresponds to a period of 5.37 days. The official period of delta Cephei, as aggregated by SIMBAD (`http://simbad.u-strasbg.fr/simbad`), is 5.3663. Clearly our findings agree very well with the professional values. The precision of our measurement could be increased by expanding in smaller regions around 5.37, but this would have little meaning relative to the accuracy with which the measurements were

Table 2: Measured and accepted periods of additional stars.

Star	Type	Estimated Period (Days)	Accepted Period (Days)	Difference (days)	Bin Size (days)	No. of Observations
T Hor	Mira	217.39	217.22	0.17	0.5	8364
S CMi	Mira	333.33	332.2	1.13	0.5	22364
R Pic	Mira	170.43	164.2 (variable)	6.23	0.5	13368
R Hor	Mira	404.71	402.67	2.04	0.5	13848
R And	Mira	410.15	408.97	1.18	0.5	26710
Omicron Cet	Mira	333.22	331.65	1.57	0.5	63555
Delta Cep	Cepheid	5.37	5.37	0.00	0.5	35624
SU Cas	Cepheid	2.04	1.95	0.09	0.2	10748
RX Cam	Cepheid	7.91	7.91	0.00	0.5	3269
SZ Tau	Cepheid	3.15	3.15	0.01	0.5	1725

made. The precision would also depend on the total span of the data — to measure to a precision of 0.001 of a day, we would have to sample for at least 2000 days. This is not a problem for Delta Cephei, as observations extend into the 1700s.

To acquire some confidence in our method, the same analysis procedure was applied to a number of other stars. As can be seen in Table 2, our results consistently were in good agreement with professional determinations of the period.

Discussion

Our approach was quite successful, but there are a number of improvements that could be made to our analysis. The processing was performed on completely unfiltered data. Data initially screened for blatant outliers and large gaps potentially could provide even greater accuracy. Better methods of interpolating empty bins could also be explored and their effects quantified.

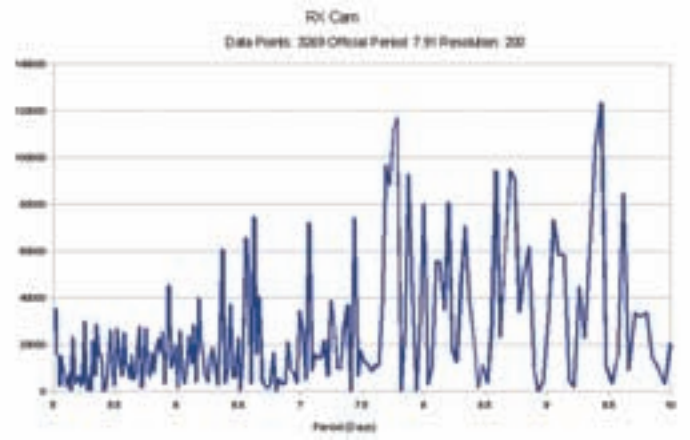

Figure 5 — RX Cam Lower Resolution

A detailed statistical error analysis could be performed, taking into account the possible variation in individual measurements as well as the total number of measurements. Some measurements have an error value supplied by the observer, but most do not and estimates must be made. This process could be used to explore the relationship between the quantity of measurements and the accuracy of the results (taking the professional values as baseline standards).

The selection of the various expansion parameters such as bin size and resolution could also be standardized. As a demonstration of the large effect these variables can have, we compare Figure 5 with Figure 6. Both plots were produced over the same period range with the same dataset. The only difference was the increase in the resolution for Figure 6. This suggests that care must be taken when expanding any given period range. If the large spike happens to lie entirely between two data points, the expansion will miss the signal entirely. In fact, if we approximate our signal as a Gaussian function, a narrower peak would correspond to a clearer signal. So, the better the measurement, the harder it is to find. At this point, knowledge of the expected result and visual inspection become an invaluable help in troubleshooting the problem. The visual plots can show, at a glance, if a clear signal is emerging from the data or has been missed.

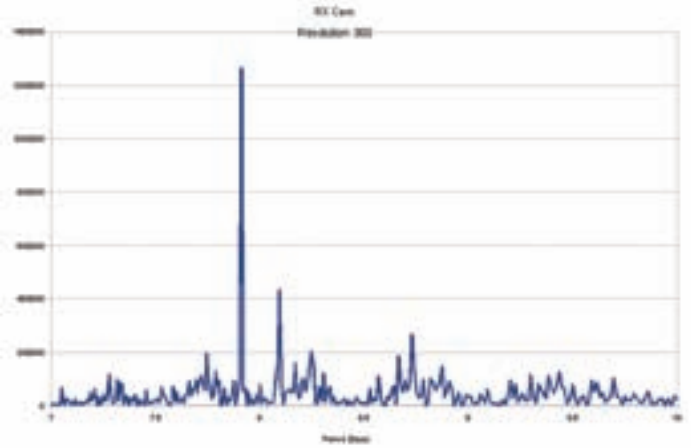

Figure 6 — RX Cam Higher Resolution

Conclusion

Although individually each measurement in the AAVSO database may contain significant error, taken as a whole, the data can be coaxed into giving us an accurate measurement of the period. Of significant note is the free nature of the tools and data used, allowing any interested party to make their own measurements. Any parties interested in a copy of the Java code used in this work are encouraged

to contact the first author by email. Overall, we conclude that this method of analysis gives a good estimate of the period of a variable star, and that the AAVSO database provides an excellent resource for further study.

Cody Friesen is an Honours Physics undergraduate at the University of Manitoba. New to astronomy, he grew up in a rural area with an excellent view of the stars. Jennifer West is an instructor and Ph.D. candidate at the university, and a member of the Winnipeg Centre.

Acknowledgments

We acknowledge with thanks the variable-star observations from the AAVSO International Database contributed by observers worldwide and used in this research.

This research has made use of the SIMBAD database, operated at CDS, Strasbourg, France. (`http://simbad.u-strasbg.fr/simbad/`)

References:

Birney, D.S., Gonzalez, G., & Oesper, D. (2006). *Observational Astronomy* (2nd ed.)

Boas, M.L. (2006). *Mathematical Methods in the Physical Sciences* (3rd ed.)

AAVSO: The AAVSO International Database: `www.aavso.org/data/overview.shtml`

On Another Wavelength

by David Garner, Kitchener-Waterloo Centre (jusloe1@wightman.ca)

HII Regions in Sagittarius: the Lagoon and the Trifid

As summer observing goes, there are two nebulae that are always worth a look, even more so when you have the nebular details in your mind while your eye gazes over them. Both are located in the constellation Sagittarius and are relatively easy to find. The Lagoon Nebula, also known as M8, is a giant emission nebula, the larger of the two, and visible with binoculars. The other, the Trifid Nebula, (M20), is a little north of the Lagoon.

The Lagoon Nebula is an extended HII region that is immersed in a giant molecular cloud. It contains dark nebulae, with globules scattered throughout (large collapsing clouds of protostellar material). As you can see in Figure 1, one of the most pronounced features in the Lagoon is a dark lane that splits the nebula from NE to SW, giving M8 its popular name.

In addition to its nebulosity, M8 contains an open cluster of OB type stars (NGC 6530). The UV light responsible for the ionization of the nebula originates primarily in three of the O-type stars: 9 Sagitarii, HD 165052, and Herschel 36. At an estimated age of 10,000 years, Herschel 36 is the youngest known main-sequence star. The strong UV radiation from Herschel 36 has developed a distinctive bipolar region known as the Hourglass Nebula (named by Sir John Herschel). This open cluster also contains more than 60 B-type stars, far more than the Orion Nebula cluster.

There is some debate as to who first discovered the Lagoon Nebula. The nebulosity was first described by Giovanni Hodierna around 1654, but was also catalogued by several others, sometimes as a nebula and sometimes as a cluster. The others include John Flamsteed (1680), Guillaume Le Gentil (1747), and Charles

Figure 1 — The Lagoon and Trifid Nebulae, courtesy of Ron Brecher, K-W Centre. This image is composed of 20 two-minute light frames taken with a QHY8 camera (Gain=0; Offset=125), a UV/IR filter, and a 4-inch f/6 refractor on a Vixen GP-DX mount. No guiding. Light frames were calibrated with 16 darks (bad pixel mapping only), 50 flats, and 50 bias frames. The calibration, grading, normalization, alignment, and stacking were done in *Images Plus 3.0*. The stacked image was processed in *PixInsight* — final tweaks were made in *Photoshop*. Shot from the Huronia Star Party, near Duntroon, Ontario. Four amazing nights of clear skies!

Messier (1764). The latter placing it as number 8 in his now-famous catalogue of non-cometary objects.

The Lagoon Nebula has an apparent size of 90×40 arcminutes, which is about three times wider than the apparent diameter of the full Moon. There is some uncertainty as to the distance to the Lagoon, with estimates varying from 4800 to 5200 light-years, with the angular size, therefore, translating to the approximate dimension of 110 by 50 light-years.

The Trifid Nebula (M20), located approximately two degrees northwest of the Lagoon in Sagittarius, is also an HII region. It was discovered by Charles Messier in 1764, but named by Sir John Herschel. The name "Trifid" means "divided into three lobes." This object is a combination of a red emission nebula around an open cluster of stars, a dark nebula that divides the emission nebula into three lobes, and a blue reflection nebula that shines above.

The red emission nebula contains a bright blue star cluster (NGC 6514) near its centre. The ultraviolet light from the stars in this cluster ionize the surrounding hydrogen gas, causing it to emit the characteristic red hydrogen-alpha light. Farther out, the UV radiation is too weak to ionize the hydrogen gas, and so, instead, the gas appears blue as it reflects the original ultraviolet light.

Distance estimates to the Trifid Nebula vary considerably, from 2700 to 7600 light-years, though a distance of about 4000 light-years is generally accepted. Although slightly dimmer and somewhat smaller than the Lagoon Nebula, the Trifid can be easily seen with a small telescope. Look for the Lagoon at right ascension $18^h\ 03^m\ 37^s$ and declination –24° 23' 12". The Trifid can be found at right ascension $18^h\ 02^m\ 23^s$ and declination –23° 01' 48". Check the map in Figure 2 to get started.

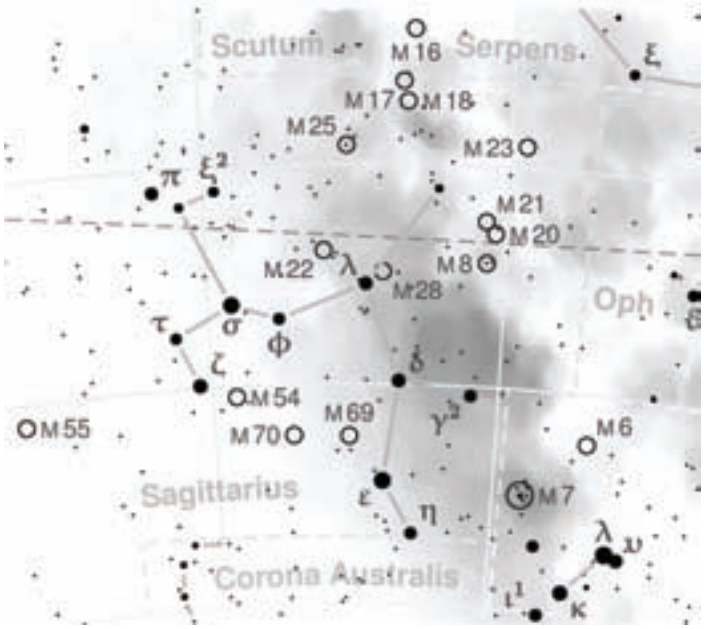

Figure 2 — A map of the constellation Sagittarius.

Dave Garner teaches astronomy at Conestoga College in Kitchener, Ontario, and is a Past President of the K-W Centre of the RASC. He enjoys observing both deep-sky and Solar System objects, and especially trying to understand their inner workings.

Second Light

by Leslie J. Sage (l.sage@us.nature.com)

An Occultation with a Difference

Most amateur astronomers are familiar with the concept of occultation, where a nearby body (*i.e.* the Moon, the Galilean moons of Jupiter, planets, and larger asteroids from the main belt) passes through the line of sight to a distant star, obscuring the light for a period from seconds up to an hour (for the Moon). There are numerous tables for times and durations of these occultations in the *Observer's Handbook*. There are no standard tables for occultations for any Kuiper Belt object other than Pluto, which makes the recent paper (see the 2010 June 17 issue of *Nature*) by Jim Elliot of MIT and his colleagues from around the world quite remarkable. They managed to capture the occultation of a star by KBO 55636 (also known as 2002 TX_{300}) on 2009 October 9. They found that it is both smaller than previously thought, and very reflective, with a geometric albedo of 0.88 (1.0 would be a perfect reflector).

The Kuiper Belt is composed of bodies outside the orbit of Neptune, with the largest being Eris and Pluto. Over 70,000 with diameters larger than ~100 km are thought to exist and over 1000 have been found since the first discovery back in 1992. KBO 55636 is a member of the Haumea family of objects, meaning that its orbit is very similar to that of Haumea, which is a roughly Pluto-sized body with a diameter estimated to be ~1500-2000 km, where different axes have different sizes, using an albedo estimated to be ~0.73. Before these observations, the only constraint on the size of 55636 was an upper limit of 420 km for the diameter.

Because of the Kuiper Belt objects' large distances from the Sun (~30 AU to ~55 AU), their orbital motion is slow and their orbital elements are not known with the precision of bodies in the inner Solar System. That makes predicting when and where occultations might occur rather tricky. Usually, the uncertainty in the prediction of the locations on Earth where the event will occur is several hundred km, meaning that even when a telescope is in the predicted zone, it might or might not see the event.

KBO 55636 was predicted to occult the star 55636.20091009 (also known as 2UCAC 41650964) October 9 at or near the locations of seven observing stations from Nicaragua to northern Australia, with the centre of the predicted zone near Mauna Kea on the Big Island of Hawaii. In the end, only two stations saw the occultation — the 2.0-m Faulkes North telescope at Haleakala on Maui, and a 0.36-m portable telescope at the visitor's centre on Mauna Kea. The stations in Nicaragua, Mexico, and at Cairns in Australia were clouded out. No occultations were seen at Leeward Community College on Oahu, or at Townsville, Australia (they were outside the predicted zone). The best data came from the Haleakala station

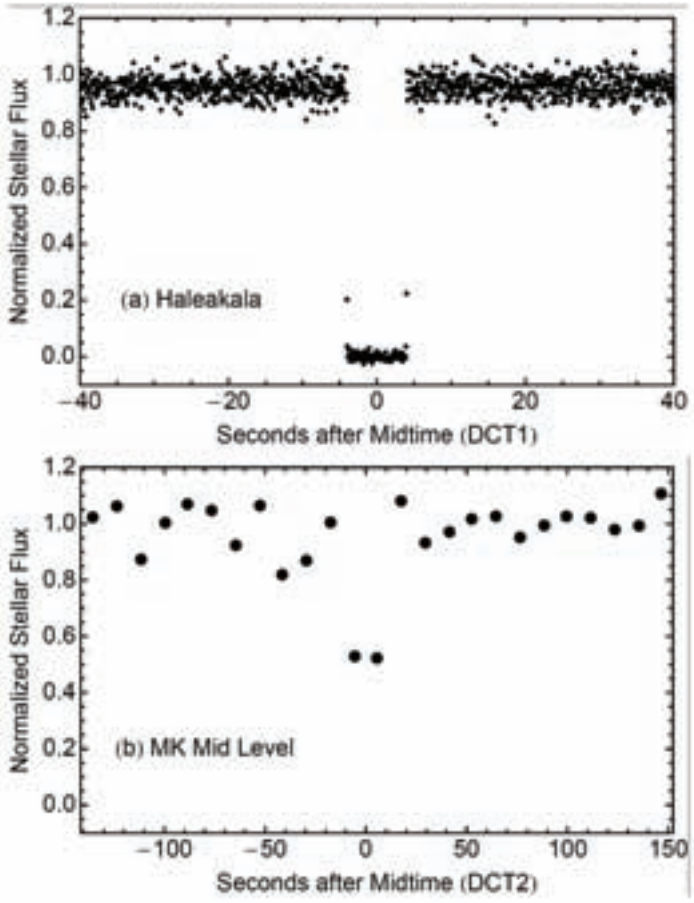

The light curves from a) the Faulkes North 2-m telescope, and b) the 0.36-m portable telescope at the Mauna Kea visitor's centre. Figures courtesy of Jim Elliot and *Nature*.

(see the light curves in the figure), but the Mauna Kea data were vital in determining the radius of 55636. Wayne Rosing (who founded the Las Cumbres Observatory Global Telescope Network — `www.lcogt.net`) was the observer at Haleakala, while Nathan Secrest was the observer at Mauna Kea.

Based upon the data, Elliot calculated a diameter of 286 km — substantially smaller than expected — and an albedo of 0.88. This makes 55636 one of the most reflective bodies in the Solar System! For comparison, the Moon's albedo is 0.136, and Venus' is 0.65. Given that the Haumea family members have deep water-absorption bands in their infrared spectra, the likely cause of the high reflectivity is a coating of water ice. If Haumea has the same albedo as 55636, then its diameter decreases to ~1200 km, which is about half the size of Pluto.

The high albedo may pose a problem for our understanding of the Haumea family. The "collisional age" — the time since the collision that created the family — is estimated to be about a billion years. The surface age was previously estimated to be ~100 million years.

Many processes (dust accumulation, "space weathering") tend to make bodies darker with time. The exceptions are bodies with atmospheres that can refresh the icy surface (Pluto, Triton) or those experiencing cryovolcanism, such as Saturn's satellite Enceladus, which requires a source of heat that would not be present near 55636. One possibility is that 55636 is essentially pure ice all the way through, and that small collisions keep the surface fresh. Haumea might possibly have a thin atmosphere that keeps refreshing the surface. But, those suggestions seem rather implausible on their own, and for both to be true would be quite surprising.

Now that the team has been assembled, we can look forward to more occultations, through which we will expand our knowledge of KBOs. This might become an area to which amateurs can usefully contribute to professional work, just as with variable stars and gamma-ray bursts. Any amateurs who want to be involved in future occultations are warmly invited. The Web site with the predicted times and locations of KBO occultations is at `http://occult.mit.edu/research/occultationPredictions.php`.

Leslie J. Sage is Senior Editor, Physical Sciences, for Nature Magazine *and a Research Associate in the Astronomy Department at the University of Maryland. He grew up in Burlington, Ontario, where even the bright lights of Toronto did not dim his enthusiasm for astronomy. Currently he studies molecular gas and star formation in galaxies, particularly interacting ones, but is not above looking at a humble planetary object.*

Through My Eyepiece

By Geoff Gaherty, Toronto Centre (geoff@foxmead.ca)

Thunderstorms and Telescopes

I'm sitting in my living room watching a magnificent thunderstorm rolling in off Georgian Bay.

Isabel Williamson maintained that every astronomer should also study meteorology so that if the weather prevented an astronomical observation, one could always study the weather itself. This seems to be the case, judging by the number of professional meteorologists who are members of the RASC, including our esteemed Editor, and by the number of RASC members who share a keen interest in the weather, either on Earth or on other planets.

My retirement home was largely chosen for its fine, dark skies. But, its location on a flood plain a few kilometres from Georgian Bay makes it a great place to watch the weather. This evening, there are orange flashes of lightning all around, accompanied by attacks and rolls on the tympani worthy of Beethoven or Berlioz, along with occasional thumps on the bass drum.

Which somehow gets me thinking about telescopes, in particular the perennial question of what is the *best* telescope?

My favourite definition says that the best telescope *for you* is the telescope *you* will use the most. That makes it very much a personal definition.

For me, there are three. The first is my "Swiss army knife": my 10×50 binoculars. These are always close at hand for wildlife observation during the day and around my neck every night under the sky. Recently we've started an astronomy club here in Orillia, and

I'm encouraging our members, most of whom are new to astronomy, to try the RASC's "Explore the Universe" program, and have joined them in doing it formally myself, using my eyes and my 10x50s. I was a beta tester for the program when it was originally proposed but never formally completed it. As Ray Bradbury said, "It is good to renew one's wonder." I've owned many different sizes of binoculars, but these 10×50s are by far my favourite for both astronomy and general use. Big enough to show lots, but light to carry and easy to hand hold.

Figure 1 — 10x50 binoculars

Number two is my Coronado Personal Solar Telescope, or "PST." With 40-mm aperture, it is my smallest telescope, yet it sees use nearly every clear day, scanning the surface of the Sun for flares and filaments, and the edge of the Sun for prominences. Some people find it hard to justify a "single use" telescope, yet I have become addicted to the dynamics of our nearest star: always something new going on.

Figure 2 — The PSP

Number three is my "big gun." Sitting inside its SkyShed POD, ready to go at a moment's notice, is my 11-inch Celestron CPC 1100 Schmidt-Cassegrain. Its massive GoTo mount is both solid and accurate, laying in my favourite variable stars and deep-sky objects precisely in the middle of the low-power field, time after time after time. Although optically not as fine as my 11-inch Starmaster Dobsonian, it wins out in convenience, with its eyepiece never moving more than a foot or two as it ranges all over the sky.

Figure 3 — The Celestron CPC 1100

Although I have many other telescopes ranging in size between these two extremes of 40 mm and 280 mm, these are the two on which I log the most time, along with my 10×50 binoculars.

An auxiliary question to the one about the best telescope is about the best telescope for urban observing. Over the years, a myth has developed that large aperture, short-focal-ratio telescopes are only good for deep-sky observing from dark-sky sites, and that city observers should choose small refractors. On the contrary, I found when I was living in downtown Toronto that I did best with the biggest fastest telescope in my arsenal, my 11-inch f/4.3 Starmaster Newtonian. Focal ratio is irrelevant in a visual telescope, except insofar as it determines your choice of eyepieces. But size always matters, no matter what the light-pollution situation.

The thunderstorm has now passed, and clear skies will be returning soon. It's great to have a choice!

Geoff Gaherty recently received the Toronto Centre's Ostrander-Ramsay Award for excellence in writing, specifically for his JRASC *column, Through My Eyepiece. Despite cold in the winter and mosquitoes in the summer, he still manages to pursue a variety of observations, particularly of Jupiter and variable stars. Besides this column, he writes regularly for the* Starry Night Times. *He recently started writing a weekly column on the Space.com Web site.*

Gizmos

by Don van Akker, Victoria Centre (dvanakker@gmail.com)

Frost on the Windows

If you are old enough and if you were cold enough, you will remember frost on the windows — on the inside of the windows. It made beautiful patterns, but when you could see your breath as you climbed out of bed, those patterns were hard to appreciate.

They still are. Especially when the window is in front of your CCD and the patterns are showing up on your images — a lovely filigree creeping in from the edges of the frame, making wonderful images...for a craft fair maybe. This happens to me once a year or so, and when it does, imaging is over. There is only one cure. The desiccant inside the camera needs to be baked. SBIG makes this sound easy: four hours in an oven at 350 °F.

But, our place on Salt Spring Island is off the grid, and the solar panels that power the observatory just can't do it for something like this. The propane oven makes water vapour as a by-product, and the wood stove has no temperature control.

Our solution isn't exactly elegant but it works well, uses only about 100 watts of generator power, and is a great conversation piece, since no one yet has successfully figured out what it's for. Guesses range from homemade espresso machine to asparagus cooker. Trouble is, when I tell them it's a desiccant oven, they are not generally a whole lot wiser.

Figure 1 — The three main components of the desiccant oven. That metal thing under the lamp base is an octagon box. It's not really optional because it provides a fireproof enclosure for your electrical connections.

The electrical bits and the oven thermometer were the only things we had to buy. All the other parts came out of the junk drawer or the recycling bin.

The idea is pretty basic and there are probably many ways it could have been done. In our version, the smaller can encloses the light bulb and stimulates airflow through the holes around the perimeter of the top. A holder for the desiccant plug rests on top of this can and allows airflow completely around the plug for even heat. A second, larger can, with a vent hole cut in the end, covers everything. The top of it — the part that forms the oven chamber — is pierced by the oven thermometer, and that's about it.

Figure 2 — The inner can in place. Note the double row of holes around the perimeter of the top. The holder for the desiccant plug could be cut and bent out of a tin can. It doesn't need to be fancy, just needs to allow airflow around the plug.

A couple of things to think about if you try something like this.

If you are not comfortable working with line-voltage electricity, get help. The potential hazards are so great that it is just not worth fooling around.

Use this outside only. It gets hot and is a fire hazard if set up too close to something flammable. As well, it will make smoke at first as the epoxy coatings burn off the inside of the small can.

Figure 3 — The desiccant cooker in use. If I hadn't left this to the last minute, I would have had time to bring it up to temperature for the photograph.

Make sure the cans are up off the lamp base a little. The lamp base should be one of the porcelain ones as the plastic one I used first couldn't take the heat. Keep a close eye on it when operating. Don't let it get too hot. You control the temperature by moving aside the lid on top to open the vent and increase the airflow. When you get it just right, the temperature will be quite stable. After four hours, turn off the power and remove the large can to let things cool. I don't wait long before screwing the plug back into the camera, letting it cool only to the point where I can just hold it in my bare hands. Any hotter might damage the rubber O-ring; any cooler, and the desiccant might start picking up moisture from the air.

Before you try out your version, of course, read the instructions that came with your camera.

Don van Akker and his observing partner, Elizabeth, are members of the Victoria Centre of the RASC. Don was proudly defiant when told he could have done this much more easily with a toaster oven. Reach him at dvanakker@gmail.com.

Gerry's Meanderings

by Gerry Smerchanski
Winnipeg Centre (smerch@mts.net)

The Bane of Our Existence — Department-Store Refractors

Few subjects in astronomy have been the object of more derision and acrimony than the ubiquitous "department store" telescope. These small telescopes come in colourful boxes covered with pictures promising magnificent views of planets and galaxies as fine as any *Hubble* image. One of the main selling points of these instruments is the claim to a very optimistic magnification, which they are supposed to be capable of achieving in spite of their inexpensive price. Most of us have experienced these "introductory" telescopes on our way to getting involved with astronomy, and even continue to help and ultimately console those who come to us asking for help in using such instruments. I have heard it claimed that these demon scopes have done more to dissuade people from pursuing astronomy even more than our weather. What exactly are the issues that have created such a nasty reputation for these rather innocent-looking telescopes, and how have they fared through our recent history?

One of the central themes throughout my reviews has been to document some of the changes in technology and equipment that have transpired in recent years, and this dissertation will be no different. So, for today's comparison, we have a rather modern equatorially mounted 60-mm refractor and an old 60-mm alt/azimuth-mounted refractor from the 1960s. 60-mm long-focal-length refractors are the epitome of department-store telescopes and many of you might see something of your own first instruments in my examples.

These two telescopes had much in common. Both had 60-mm achromatic objectives of 750-mm focal length. This combination of a relatively small objective with a long focal length has been a common format for beginner telescopes. The long-focal-length achromatic objectives — in this case an f-ratio of 12.5 — can produce relatively decent views without resorting to more expensive glass. Both telescopes used 0.965-inch eyepieces, diagonals, and Barlows — a format that was (and is) common in Japan, as compared to the popular 1.25-inch format used in North America and Europe. Both telescopes were provided with either alt/azimuth or equatorial mounts, and both employed small finderscopes with cross hairs.

Figure 1 — The relatively new Bushnell 60-mm refractor and its 40-year-old counterpart.

Just about the only difference that one could detect immediately after 40 years of evolution was in the materials used to execute this classic design. The old Scope refractor (think of it as a Tasco clone prevalent during the '60s) was made entirely out of metal with no plastic in sight. The stampings indicate that all assemblies were made in Japan, as was common for bargain scopes of that vintage. The newer Bushnell scope also had a metal tube but almost everything else — the focuser assembly, the dew cap and lens cell, and drawtube — were made of plastic. This gave the newer scope a low-quality feel compared to the rigid structure of the old unit. Those people who have experienced automobiles of that earlier era will know firsthand of this difference in feel.

But, the issue with these telescopes has always been their performance — or lack thereof. There are two general problems that plague these scopes. The first is the absence of mechanical precision and capacity to maintain a properly aligned optical train. I found that focuser slop and drawtube droop were chronic problems when the tubes were extended to achieve focus. Nevertheless, both telescopes performed acceptably provided no heavy-weight eyepieces were used — so forget about attaching cameras without making serious modifications.

The second issue concerned the quality of the optics provided, and especially the notorious eyepieces that often were made with plastic lenses. Surprisingly, the objective lenses tested fairly well, providing good results during star tests when used with decent eyepieces. It is this adequate performance by the objectives that points the way to using these telescopes effectively.

The way to make the best use of department-store telescopes is to abandon the supplied eyepieces and use either good quality 0.965-format eyepieces (which are rather rare in North America) or employ a hybrid diagonal that allows the use of the better-known 1.25-inch eyepieces that you might have in your equipment box. The best 0.965 eyepieces encountered these days are the rather expensive ones made by Takahashi, but using an eyepiece that costs more than the scope defeats the purpose of observing on a budget. There are some rather good, inexpensive, simple Kellner and Orthoscopic 0.965-format eyepieces, but they are rather rare and also would not be a general solution for most owners who plan to upgrade at some point. Seibert Optics has a line of 0.965 eyepieces featuring a 65-degree apparent field of view that are claimed to be superior to department-store eyepieces, but they weren't available for testing.

The more promising route for owners of these scopes, who own or intend to purchase 1.25-inch eyepieces, is to acquire a hybrid diagonal and substitute the larger-sized eyepieces when observing. I compared the view using some rather good 0.965 JSO eyepieces to the view using a hybrid diagonal and regular 1.25-inch Plössls. There was little difference in performance, but the larger field of view of the Plössls was apparent and appreciated. With

modest field-of-view 1.25-inch eyepieces (50 to 60 degrees), there was no evidence of vignetting, but those with a wider apparent field might have some problems with light fall-off at the edges of the field.

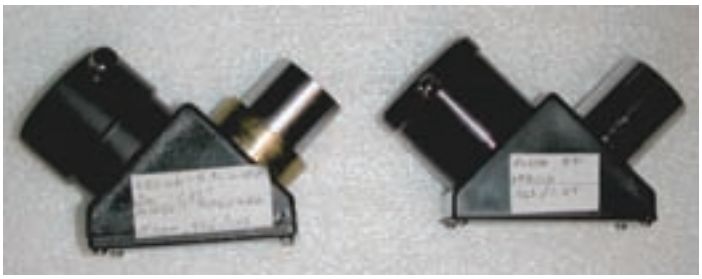

Figure 2 — Hybrid diagonals allow 1.25" eyepieces. Left: dual use fits 1.25 and 0.965 drawtubes.

Using the Scopes

The actual testing revealed some surprising results. Despite the similarities of the two scopes, the image in the older version was decidedly brighter, revealing the faintest stars more readily than the newer Bushnell. At low power, both scopes had clean star images that were fairly crisp across the entire field of view — one of the benefits of the long focal length. However, as the power was increased to view planets, the older scope showed much false colour; Saturn even took on a rainbow hue. The newer Bushnell scope showed a much less coloured image. The plastic housing even proved to be able to resist dewing; on several evenings, the metal-clad Scope objective fogged over while the plastic-mounted Bushnell objective remained mist-free.

The finderscopes were frustrating in being small and dim and having poor-quality images. The finder for the Bushnell, held by a plastic mount, had trouble holding position from day to day and required alignment before each session. The older Scope's all-metal holder worked well, but it was a right-angle finder and not quite as useful for quick sighting. With long, thin telescopes, one is tempted to forego a finder and merely sight along the tube, but the narrow field of view and the slop in both mounts makes this a futile exercise. Both of these scopes would benefit from a red-dot zero-power finder. (The latest version of the Bushnell does have just such a focuser.)

The mounts also proved to be source of frustration as there was slop in most axes. While the mounts could hold the scopes, their slow-motion controls were neither smooth nor linear. The newer equatorial mount with the Bushnell had an inexcusable problem with locking screws that ran into other parts of the mount and prohibited free rotation in several orientations. It's understandable why these scopes end up being used as guide scopes or put on other more competent mounts. The supplied mounts work, but the user must accept certain annoying quirks and limitations.

I couldn't recommend buying one of these telescopes, but if you obtained one cheaply or if you already have one, employing a hybrid diagonal and putting some effort to reduce the slop, replacing some of the locking hardware, and adding a zero-power finder would go a long way toward making them acceptable as low-powered telescopes. But, these days, we are blessed with a plethora of inexpensive short-focal-length rich-field telescopes that can do a better job at low power than these older designs. It seems that department-store refractors are

Figure 3 — Superior coating on the older glass (left) results in a dimmer reflection and better light transmission.

going to be with us for some time, but they will be remembered as telescopes that offered more promise than they could deliver. It didn't have to be that way, but such is the world where economics intersects astronomy.

Gerry Smerchanski is an eclectic member of the Winnipeg Centre whose basement is stuffed with all manner of old telescopes, binoculars, and other optical gear, including several department-store telescopes. He can often be found expounding on the mysteries of optical design and any other subject over a beer.

Astrocryptic

by Curt Nason

The solution to last issue's puzzle

The RASC at the Canada-Wide Science Fair

by John Crossen (johnstargazer@xplornet.com)

Take 494 of Canada's brightest high-school science students and pour them into Peterborough, Ontario's Evinrude Centre. Separate into junior, intermediate, and senior levels. Now mix thoroughly with a like number of judges and let simmer for two days. The end result will tickle the taste buds of any science buff.

Two days of judging projects impressed me with the variety of subjects that captured the imaginations of young scientists. Projects ranged from a myriad of innovative solutions for environmental and health issues to robotics, maximizing solar energy, and experiments with optics and polarization.

The enthusiasm these young scientists conveyed as they talked about how they originated their hypotheses and designed their experiments was impressive. From employing good test methodology with control groups to closely monitored variables, their work was remarkable.

Sometimes the project failed. But failure or success wasn't the point. What was important was gaining a deeper understanding of their subject and properly engaging the scientific process to arrive at a final truth — whether it was positive or negative.

While there were no pure astronomy projects in the 450 that were presented, two young scientists applied astronomical principles to their projects to the point that they were deemed eligible for the RASC Astronomy Awards.

Sarah Battat of Montréal presented an interesting experiment with polarization that had some applications in the field of astronomy. In addition to the RASC award, her project, entitled *Ray Ray Go Away,* was a Gold Award Winner in the Physical and Mathematical Sciences category, Intermediate Division.

Figure 1 — Only the Sun could beam brighter than the smile on Loral Christie's face. Her project *The Brightest Path* used the ecliptic as one element in maximizing the efficiency of solar panels.

Figure 2 — Sarah Battat of Montreal was awarded the RASC's "Excellence in Astronomy" prize in the Intermediate category.

The Brightest Path was the title of Loral Christie's project. She used the ecliptic as a factor in positioning an array of solar panels to maximize their efficiency. Loral, who is from Blue Water, Ontario, also took home a Silver Award in the Junior Division of the Physical and Mathematical Sciences category. Along with their RASC cash awards, both young scientists received one-year youth memberships in the RASC.

When the excitement and emotion of the CWSF settled down and I had a few moments to relax and reflect on what I had been a part of, a large and very contented smile crossed my face. I felt very proud of this generation of young scientists, whatever their chosen discipline. Canada's future is in some young and very capable hands.

John Crossen owns Buckhorn Observatory (`buckhornobservatory.com`). *Come see what's up.*

Figure 3 — With 494 young scientists tending 450 displays, the display floor was alive with excitement and youthful energy.

Figure 4 — The Peterborough Astronomical Association teamed up with Buckhorn Observatory to give the students a tour of the constellations and some solar viewing.

Reviews/Critiques

Luise Herzberg, Astrophysicist: A Memoir, by Paul A. Herzberg, pages 161, 13 cm × 18 cm, York University Bookstore, 2010. Price $27.95, paperback (ISBN-13: 978-1-55014-511-3).

The name Gerhard Herzberg (1904-99) is well-known, of course, as he is one of only ten Canadian scientists to win a Nobel Prize. Even though he received the prize in chemistry for his research on molecular free radicals, astronomers consider him one of their own because of the astrophysical implications of his spectroscopic studies and for his work on planetary atmospheres, comets, and interstellar matter. The Herzberg Institute of Astrophysics, the organization responsible for Canadian government astronomy, was named in his honor in 1975. Within the RASC, he was a longtime member, occasional speaker, and contributor to the *Journal,* and eventually Honorary President. The story of his life was recently told in a masterful biography by his physicist colleague, Boris Stoicheff (2002 *Gerhard Herzberg: An Illustrious Life in Science,* NRC Press, Ottawa), who naturally called on Herzberg's children, Agnes and Paul, and Herzberg's second wife, Monika, for family memories and photographs. Herzberg's first wife, Luise, died in 1971, and Stoicheff frequently mentioned her in his book. He did not give her a major role since the book was, after all, a biography of Gerhard.

It is safe to say that few Canadians, let alone astronomers, know anything about the career of Luise Herzberg (1906-71). As far as the RASC is concerned, her name occasionally shows up in the *Journal* in the 1950s as part of reports from the Dominion Observatory, where she did solar research with Jack Locke and Vic Gaizauskas. In *Luise Herzberg, Astrophysicist,* her son Paul Herzberg has set out to put on record her remarkable achievements. In spite of many obstacles, Luise authored or co-authored 31 scientific contributions, almost all in spectroscopy. Because of her solar work at Yerkes Observatory in the United States and at the Dominion Observatory in Ottawa, Paul has chosen to call his mother an astrophysicist in his title, but her work (as with Gerhard's) embraced several disciplines, from molecular chemistry to geophysics. The last 12 years of her life, when she worked at the Radio Physics Laboratory in Shirley Bay, Ottawa, were scientifically her happiest and most productive.

Luise Oettinger and Gerhard Herzberg were both born in Germany and met there as students. They were married in 1929 and she received her Ph.D. in 1933, while Gerhard worked as a Privatdozent at the Technische Hochschule in Darmstadt. In the same year, Hitler became Chancellor and almost immediately began introducing anti-Semitic measures. Though neither Luise nor Gerhard were religious people, her parents were Jewish, and so the Nazi policies applied to both of them. As a consequence, Gerhard lost his teaching job when a 1934 law required all academic staff to prove that their wives were "Aryan." One can only imagine what their fate might have been if it had not been for the efforts of John Spinks, a young faculty member from the University of Saskatchewan, who not only happened to be doing research with Gerhard but was also living in the same house in Darmstadt. To make a long story short, the Herzbergs moved to Saskatoon in 1935, where their children were born, and Luise's parents came to live with them in 1939.

Paul provides a sympathetic picture of his mother as a frustrated scientist for most of her life, able to do only a little research because of her duties as the wife of a workaholic husband, the mother of two small children, and a daughter of demanding parents, especially her father. In addition, she catered to Gerhard's very limited vegetarian diet, entertained his colleagues, typed all his correspondence, and prepared several hundred illustrations and numerous tables for the first two volumes of his authoritative book, *Molecular Spectra and Molecular Structure.* From 1948 on, she suffered several serious bouts with breast cancer, twice requiring surgery. Yet withal she had a great sense of humour. She certainly served as an outstanding example of the old saying "behind every successful man is a great woman," yet we are left with the sad impression that Gerhard did not fully appreciate how much of his success he owed to his devoted wife.

Once the children began to grow up and her parents had passed on, Luise properly came into her own. At first, both at Yerkes and the Dominion Observatory, she had to make do with the unpaid position of "volunteer research associate." That was normal for the wife of a scientist on staff, as we know also from the example of Helen Hogg. Eventually, from 1952-58, Luise was paid, but only as a summer assistant, in spite of having her doctorate and twelve publications to her credit. Finally, in 1958 she became a scientific officer at the Observatory, and a year later at the Radio Physics Laboratory. There she studied ionospheric phenomena and analyzed data from Canada's first satellite, *Alouette.*

The part of the book that deals with this latter part of her career seems less effective to me. Perhaps that is because I was a summer student working on *Alouette* data in 1963 and knew a little of the story from the inside, though I was unaware of Luise Herzberg when I was there. In any case it is always difficult to explain complex research in simple terms, and the author circumvents that by quoting the abstracts or introductory sentences of Luise's papers themselves.

The book's true strength is in the narrative and the superb photographs that are reproduced with high resolution and great clarity. Anyone who has read Stoicheff's biography of Gerhard, needs to read Paul's story of his mother as well. Both should be read by anyone with an interest in the recent history of science in Canada. As far as I am aware, Paul Herzberg's memoir of his mother provides a unique look at a Jewish immigrant woman scientist, very much in the shadow of her famous husband, struggling to break loose from oppression of one kind or another. He has done a service to all by reminding us of the challenges faced by our forebears, and helping us to see how fortunate we are in comparison.

Peter Broughton

Peter Broughton is a Past President of the RASC and a frequent writer on the history of astronomy in Canada.

Great Images

Don van Akker shows another of his talents in this image of a summer favourite - the globular cluster M13 in Hercules. Don assembled 120 images (30x5 seconds, 30x15, 20x60, 20x120, 20x240) using an SBIG ST4000MX on a Meade 12-inch LX200 SCT. As Don says "A little overboard on the number of exposures but I get a lot of noise with that camera."

Messier 41, a winter stalwart, is an easy-to-find open cluster underneath Sirius, the brightest star. As with most open clusters, it has a population of red and blue stars, reflecting the differing rates of evolution of high- and low-mass stars. This image is made up of 20 1-minute unfiltered exposures taken by Jay Anderson in Arizona with a modified Canon 40D mounted to a TMB 5-inch refractor.

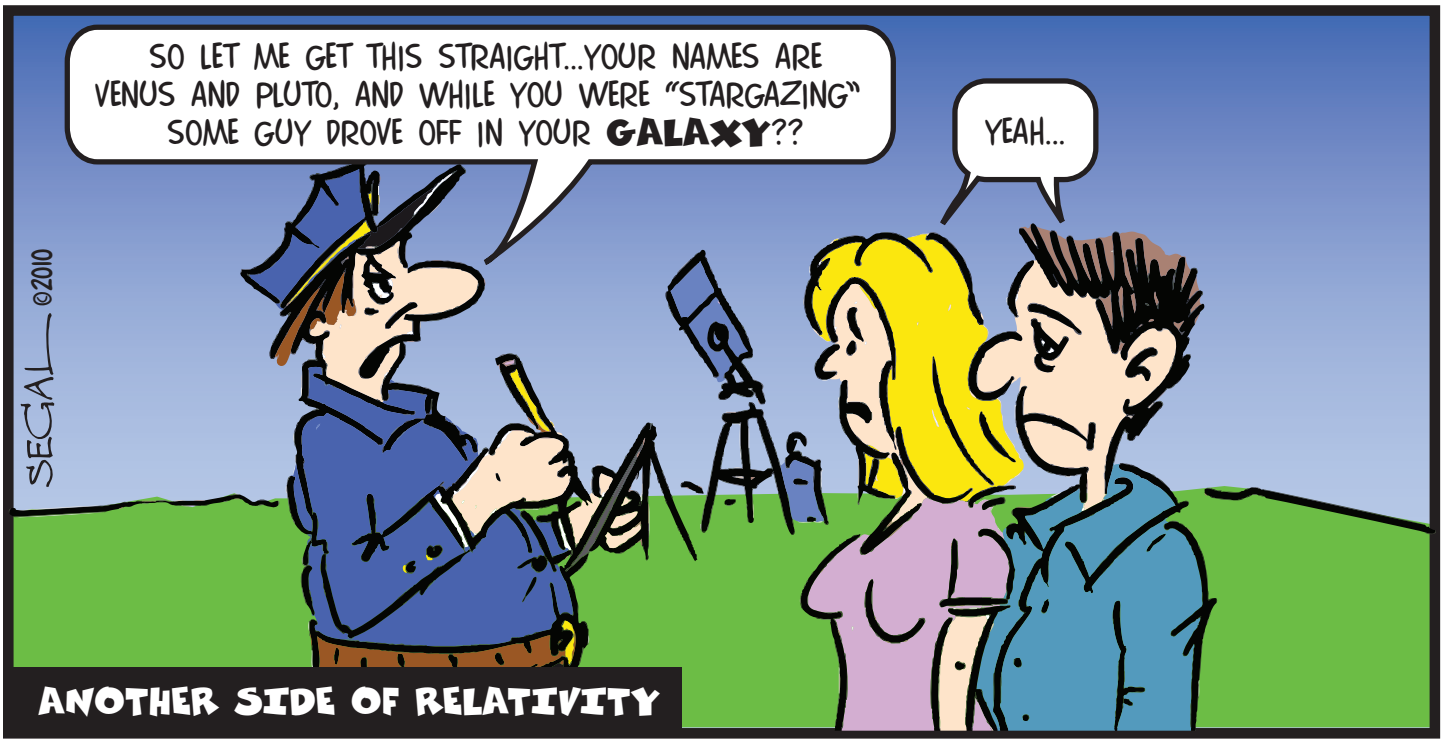

THE ROYAL ASTRONOMICAL SOCIETY OF CANADA

NATIONAL OFFICERS AND COUNCIL FOR 2010–2011/CONSEIL ET ADMINISTRATEURS NATIONAUX

Honorary President	Jim Hesser, Ph.D., Victoria
President	Mary Lou Whitehorne, Halifax
1st Vice-President	Glenn Hawley, B.Sc., B.Ed., Calgary
2nd Vice-President	Colin Haig, B.Sc., M.Sc., Hamilton
Secretary/Recorder	James Edgar, Regina
Treasurer	Mayer Tchelebon, MBA, CMA, Toronto
Past Presidents	Dave Lane, Halifax and Scott Young, B.Sc., Winnipeg
Editor of *Journal*	Jay Anderson, B.Sc., MNRM, Winnipeg
Editor of *Observer's Handbook*	Patrick Kelly, M.Sc., Halifax
Editor of *The Beginner's Observing Guide*	Leo Enright, B.A., Kingston*
Editor of *Observer's Calendar*	Dave Lane, Halifax
Executive Director	Deborah Thompson, CAE, Toronto
National Office Manager	Jo Taylor, 203 - 4920 Dundas St W, Toronto ON M9A 1B7 Telephone: (416) 924-7973

* Deceased 2009 August 11

CENTRE ADDRESSES/ADRESSES DES CENTRES

The most current contact information and Web site addresses for all Centres are available at the Society's Web site: **www.rasc.ca**

Belleville Centre
c/o Greg Lisk, 11 Robert Dr, Trenton ON K8V 6P2

Calgary Centre
c/o Telus World of Science, PO Box 2100 Stn M Location 73, Calgary AB T2P 2M5

Charlottetown Centre
c/o Brian Gorveatt, 316 N Queen Elizabeth Dr, Charlottetown PE C1A 3B5

Edmonton Centre
c/o Telus World of Science, 11211 142 St, Edmonton AB T5M 4A1

Halifax Centre
PO Box 31011, Halifax NS B3K 5T9

Hamilton Centre
576 - Concession 7 E, PO Box 1223, Waterdown ON L0R 2H0

Kingston Centre
PO Box 1793, Kingston ON K7L 5J6

Kitchener-Waterloo Centre
305 - 20 St George St, Kitchener ON N2G 2S7

London Centre
c/o Peter Jedicke, 82 Barrydale Cres, London ON N6G 2X4

Mississauga Centre
PO Box 98011, 2126 Burnhamthorpe Rd W, Mississauga ON L5L 5V4

Centre francophone de Montréal
C P 206, Station St-Michel, Montréal QC H2A 3L9

Montréal Centre
18455 Meloche St, Pierrefonds QC H9K 1N6

New Brunswick Centre
c/o Paul Gray, 1068 Kingsley Rd, Birdton NB E3A 6G4

Niagara Centre
PO Box 4040, St. Catharines ON L2R 7S3

Okanagan Centre
PO Box 20119 TCM, Kelowna BC V1Y 9H2

Ottawa Centre
1363 Woodroffe Ave, PO Box 33012, Ottawa ON K2C 3Y9

Prince George Centre
7365 Tedford Rd, Prince George BC V2N 6S2

Québec Centre
2000 Boul Montmorency, Québec QC G1J 5E7

Regina Centre
PO Box 20014, Regina SK S4P 4J7

St. John's Centre
c/o Randy Dodge, 206 Frecker Dr, St. John's NL A1E 5H9

Sarnia Centre
c/o Marty Cogswell, 6723 Pheasant Ln, Camlachie ON N0N 1E0

Saskatoon Centre
PO Box 317 RPO University, Saskatoon SK S7N 4J8

Sunshine Coast Centre
PO Box 577, Sechelt BC V0N 3AO

Thunder Bay Centre
286 Trinity Cres, Thunder Bay ON P7C 5V6

Toronto Centre
c/o Ontario Science Centre, 770 Don Mills Rd, Toronto ON M3C 1T3

Vancouver Centre
1100 Chestnut St, Vancouver BC V6J 3J9

Victoria Centre
3046 Jackson St, Victoria BC V8T 3Z8

Windsor Centre
c/o Greg Mockler, 1508 Greenwood Rd, Kingsville ON N9V 2V7

Winnipeg Centre
PO Box 2694, Winnipeg MB R3C 4B3

Great Images

Kevin Black of the Winnipeg Centre used the few hours of darkness in June to capture this image of the Milky Way from St. Malo in southern Manitoba. Local light pollution highlighted the thin clouds to give this image a three-dimensional character. Kevin used an 18-mm lens at f/4 on a Canon 5D set at 2000 ISO. Exposure was 5 minutes.